

Formation of mineral-associated organic matter via rock weathering: an experimental test for the organo-metallic glue hypothesis

Kaori Matsuoka¹, Jo Jinno¹, Hiroaki Shimada², Emi Matsumura¹, Ryo Shingubara³, [Puu-Tai Yang¹](#), Rota Wagai¹

¹Institute for Agro-Environmental Sciences, National Agriculture and Food Research Organization, Tsukuba, 305-8604, Japan

²Division of Plant Production Science, Section of Plant Production Science Research Center for Global Agromedicine, Obihiro University of Agriculture and Veterinary Medicine, Obihiro, 080-8555, Japan

³Research Center for Advanced Analysis, National Agriculture and Food Research Organization, Tsukuba, 305-8604, Japan

Correspondence: Kaori Matsuoka (matsuoka.kaori811@naro.go.jp; kaori.matsuoka@hotmail.co.jp); Rota Wagai (wagai.rota200@naro.go.jp; rota.wagai@gmail.com)

Abstract. Mineral-associated organic matter (MAOM), representing the dominant form of relatively stable carbon (C) in soil, often contains high physicochemical heterogeneity. The co-occurs with localization of organic matter (OM) with reactive iron (Fe) and aluminum (Al) and iron (Fe) phases across soils. Yet, how organo-metallic associations at the molecular scale give rise to the emergent soil properties such as aggregate formation and the persistence of organic matter (OM) in soil remains unclear. Various MAOM fractions across a range of natural and cultivated soils from five soil orders has led to the “organo-metallic glue” hypothesis. The hypothesis proposes that dissolved metal released from weathering coprecipitates formed between mineral derived metals and microbially processed OM form cohesive organo-metallic phases that bind other particles into act as a binding agent, promoting the formation of stable assemblage microaggregates and thereby enhancing soil OM persistence. However, the formation mechanism remains unclear as the observed associations reflect multiple soil processes. We tested this concept using an artificial soil system comprising thus designed a simple laboratory experiment to test if the supply of metals and metalloids through rock weathering controls MAOM formation and if the OM to metal ratio of the material formed is consistent with complexation, sorptive association, or their mixture (i.e., coprecipitates). Two end member crushed igneous rocks (fine basalt: 20–38 μm , coarse basalt and granite: and basalt) crushed to have 38–75 μm , and river sand size and, additionally, 20–38 μm size for basalt, as well as river sand (100–300 μm), as control were mixed with leaf compost and microbial inoculum, (powdered to 100–250 μm) as single OM source. The mineral-OM mixture rock-OM mixtures were incubated aerobically at 30 °C with the natural soil microbial community and subjected to eight wet and dry cycles using artificial rainwater (pH 4.73) over a 55-days experiment. Sequential density fractionation after the incubation revealed The mixtures were then fractionated by density to examine the formation of meso-density, organo-mineral assemblages aggregates (1.8–2.4 g cm^{-3} : MF) in the following order: fine basalt > coarse basalt > granite > sand. by distinguishing it from the compost dominant low density fraction (< 1.8 g cm^{-3} : LF) and high density fraction (> 2.4 g cm^{-3} : HF) consisting of the crushed rock. The accretion of C and oxalate-extractable Fe, Al, and Si in MF generally followed the same pattern. formation assessed as C content was 1.49 ± 0.06 1.3 mg C g^{-1} rock (fine basalt), 1.04 ± 0.08 0.93 (coarse basalt), and 0.62 ± 0.06 0.55 (granite) over the 55 days, while the net MF mass increase was detected only in fine basalt due to the presence of meso-density materials in the crushed rock (< 7% by mass). Faster chemical weathering of the fine basalt showed the strongest increase in was indicated by a significant increase in extractable metals, especially Fe and Al phases, in MF largely in MF, and the highest leaching of Fe and base cations (esp. Na and Ca). Enrichment of extractable Fe, Al, and Si in MF and their slight depletion from high-density fraction (> 2.4 g cm^{-3} : HF) suggest that weathering-derived metals first likely complexed or coprecipitated associated with OM, to forming The organo-metal rich phases that subsequently bound other particles to form organo-mineral

assemblages. MF aggregates formed in the fine basalt treatment had the C₂-to-metal (Fe+Al) molar ratio of 0.636 ± 0.01, consistent with organo-metal coprecipitates. Preferential incorporation of microbially-processed, N-rich OM into MF in (molar basis), consistent with organo-metal coprecipitation. Further analysis focusing on the two basalt treatments was indicated by lower revealed a significant decline in C:N ratios by 23–25 units and enrichment of δ¹³C and δ¹⁵N by 0.9–1.2% and 0.6%, respectively, relative to in MFs compared to low-density fraction (< 1.8 g cm⁻³). SEM and LFs, indicating a strong contribution of microbial N-containing compounds to the MAOM formation. While microbial community composition differed among the treatments, no significant difference was found in qPCR-based bacterial number or species richness. STXM/NEXAFS analyses of limited MF materials confirmed the presence of shaking-resistant microaggregates and the co-localization of microbially altered C with Fe and Al. Microscopic analyses using SEM and STXM confirmed the presence of shaking-resistant microaggregates and co-localization of C, Fe, and Al in MF from selected MF samples. Together, our Collectively, these -results provide experimental evidence supporting strongly supported the organo-metallic glue hypothesis and demonstrate that provided laboratory evidence of basaltic rock weathering can rapidly promote -induced MAOM formation organo-mineral assemblage formation. This mechanism links microbial processing, mineral weathering, and reactive metal dynamics, offering as well as some insights into early pedogenesis and soil OM formation under rock amendment conditions organo-mineral interactions when applying crushed rock to soils.

1 Introduction

Organic matter (OM) in soil plays a fundamental role in global carbon cycling, soil fertility, and ecosystem functioning (Lehmann et al., 2020; Friedlingstein et al., 2022; Angst et al., 2023). Its long-term persistence strongly depends on its physicochemical associations with reactive soil minerals such as aluminosilicate clays and iron (Fe) and aluminum (Al) metal oxides with that have a high specific surface area and reactivity (e.g., Sørensen, 1972; Baldock and Skjemstad, 2000; Wattel-Koekkoek et al., 2003; Saidy et al., 2015; Hemingway et al., 2019). Among these, One group of reactive minerals is pedogenic metal and metalloid phases (mainly iron (Fe)-, aluminum (Al)-, and silicon (Si)-bearing phases), formed weathering products of Fe-, Al-, and/or Si-bearing minerals during mineral weathering, are especially reactive soil development. They occur as can be present as mono or polymeric species complexed with organo-metal complexes, ie ligands or as mineral phases oxides such as short-range-ordered (SRO) aluminosilicates and metal oxides, and, to a less extent, s well as high-crystallinity metal Fe and Al oxides (e.g., Harter and Naidu, 1995; Cornell and Schwertmann, 2003; Parker, 2005; Ashida et al., 2021; Watanabe et al., 2023).

At larger macro scales, while OM molecular composition exerts some controls depending on ecosystem type and climate (Sollins et al., 1996; Hall et al., 2020), soils rich in pedogenic metals generally store more OM in soil. For instance, basaltic and andesitic soils often have been shown to accumulate greater higher OM stocks than granitic soils (Orgill et al., 2017; Angst et al., 2018; Dutta et al., 2000; Rasmussen et al., 2005; Mao et al., 2020), while OM molecular composition also exerts some controls depending on ecosystem type and climate (Sollins et al., 1996; Hall et al., 2020). Furthermore, Pedogenic Fe and Al metal contents often correlate positively correlate with soil OM stock and, to some extent, with its C persistence inferred from based on radiocarbon analysis (e.g., Torn et al., 1997; Percival et al., 2000; Masiello et al., 2004; Lawrence et al., 2015; Shimada et al., 2022; von Fromm et al., 2025). Their protective effects on OM may persist even under decades of intensive cultivation in humid tropics (Arai et al., 2024). At the the molecular scale (submicron to nano sizes), these pedogenic metals phases form engage in various association interactions with OM, including, such as hydrophobic interactions, cation bridging, adsorption, organo-metal complexation, and and coprecipitation, that thereby enhancing OM resistance to microbial degradation and dissolution (Keil and Mayer, 2014; Kleber et al., 2015). Recent spectroscopic studies revealed diverse modes of OM-mineral and OM-metal/metalloid associations. Those include coprecipitates of metal and metalloid oligomers with organics (Among these, coprecipitation remains the least understood. Although the chemical

85 composition and formation environments of coprecipitates may vary widely, conceptual advances have been made by
comparing soil-derived coprecipitates with synthetic analogs produced under soil-relevant conditions, using electron
microscopy and spectroscopy techniques (Basile-Doelsch et al., 2015; Tamrat et al., 2018, 2019; Jamoteau et al., 2023;
90 Jamoteau et al., 2025), calcium complexation (Rowley et al., 2023), and nanoscale organic layering on mineral surface
(Possinger et al., 2020; Underwood et al., 2024). However, how a remaining key question is the role of these molecular-
scale nanoscale interactions give rise to the coprecipitates on the emergence of larger-scale soil properties such as OM
persistence and hierarchical the development of aggregate/ions and soil pore structure network developments remains as a
95 fundamental question (Asano and Wagai, 2014; Regelink et al., 2015; Rabot et al., 2018; Totsche et al., 2018; Sehlüter et al.,
2020; Yudina and Kuzyakov, 2023; Amelung et al., 2024, 2023). These hierarchical soil structures, which strongly regulate
microbial and plant root activities and are thus link mineral reactivity to ecosystem functioning
(Chorover et al., 2022; Hartmann and Six, 2023; Philippot et al., 2024).

The *organo-metallic glue* hypothesis (Wagai et al., 2020) provides a conceptual bridge may offer a mechanistic bridge
95 between nanoscale mineral-organic interactions and the macro-scale aggregation, and may offer more mechanistic
interpretation on previous observations patterns (e.g., C protection within aggregates, C-metal correlations across bulk soils
and physical fractions) and the molecular-scale interactions between OM and minerals. ItThe hypothesis, proposes that Fe
and Al dissolved from minerals complex or coprecipitate with decomposing OM to form cohesive organo-metallic phases
that act as “glue”, binding mineral and organic particles into stable microaggregates. Support for this mechanism includes
100 the consistent and based on the observed co-occurrence of extractable Fe and Al phases with nitrogen (N)-enriched OM in
meso-density fractions ($MF: 1.8\text{--}2.4\text{ g cm}^{-3}$) with relatively constant OC: metal ratios found across diverse 23 soils and the
relatively constant OC:metal ratios among soil physical fractions within each soil (Wagai et al., 2020). Yet from 5 soil
orders, suggests that Fe and Al dissolved from soil minerals bind with decomposing OM to form organo-metallic glue which
binds mineral and organic particles (e.g., clays and fragmented POMs) to form physically stable microaggregates. However,
105 testing this mechanism hypothesis in using natural soils is challenging because of their compositional
heterogeneity and the influence of soils contain diverse OM compounds and multiple metal species as a result of multiple
pedogenic short and long term processes. An artificial soil system, which consists of defined mineral and OM components,
would be suitable to assess specific mechanisms under controlled conditions. Previous experiments OM mineral interactions,
as it has have shown that various mineral-organic associations demonstrated the formation of organo-mineral assemblages
110 can form rapidly within short timescales under controlled conditions (e.g., Vogel et al., 2014; Pronk et al., 2017; Bucka et al.,
2019, 2021). However, their formation mechanisms although the effect of mineralogical remain poorly
understood parameters is largely unexplored.

This current study aimed to evaluate examine some key aspects of the *organo-metallic glue* hypothesis using an artificial
soil system composed of crushed rock and leaf compost. We hypothesized that the differences in rock weathering rate, and
115 thus (i.e., the supply rate of Fe and Al,) govern controls the formation of organo-mineral assemblages in the presence of
OM. To and test this, we incubated ed it using two end-member igneous rocks (basalt and granite and basaltic rock) and
quartz crushed to have 38–75 μm size and, additionally, 20–38 μm size for basalt, as well as river sand (100–300 μm) (as a
control) with. These minerals were mixed with leaf compost (powdered to 100–250 μm) as a single OM source. Up and a
soil inoculum, subjecting ation with the soil microbial community, the mineral-OM mixture rock-OM mixtures were
120 subject to weekly leaching-drying cycles events with artificial rainwater, followed by drying over a for 55-day incubation
durations. We quantified the formation of organo-mineral aggregate assemblage was assessed via sequential by density
fractionation, elemental and extractable metal analyses, followed by chemical and, to, to a limited extent, miextent,
microscopic characterization (of isolated fractions by SEM and STXM-NEXAFS). We expected meso-density fractions to
show enrichment in extractable metals relative to low- and high-density fractions, reflecting the role of We showed
125 significant increases in both extractable metals (esp. Fe) and OM in the meso-density fraction from fine basalt-OM mixture

and discussed the linkage among weathering-derived metals in binding OM into physically-stable microaggregates, microbial heterotrophic activity, chemical weathering, and organo-mineral aggregation. List of data on figures and tables in the main text and supplementary information is presented in Table S1.

2 Materials and Methods

We prepared four types of rock-mineral-organic matter (OM) mixtures using crushed rock and river sand with leaf compost, followed by 55-day aerobic incubation with eight wet-and-dry cycles (Fig. 1). Microbial respiration was not measured. Leachates were collected for chemical composition. The mixtures after the incubation were destructively sampled and fractionated by density. Each fraction was analyzed for total C and N as well as to quantify the organo-mineral assemblage formed extractable metals and metalloids. For a selected samples and fractions, we also conducted microscopic/spectroscopic and microbial characterization.

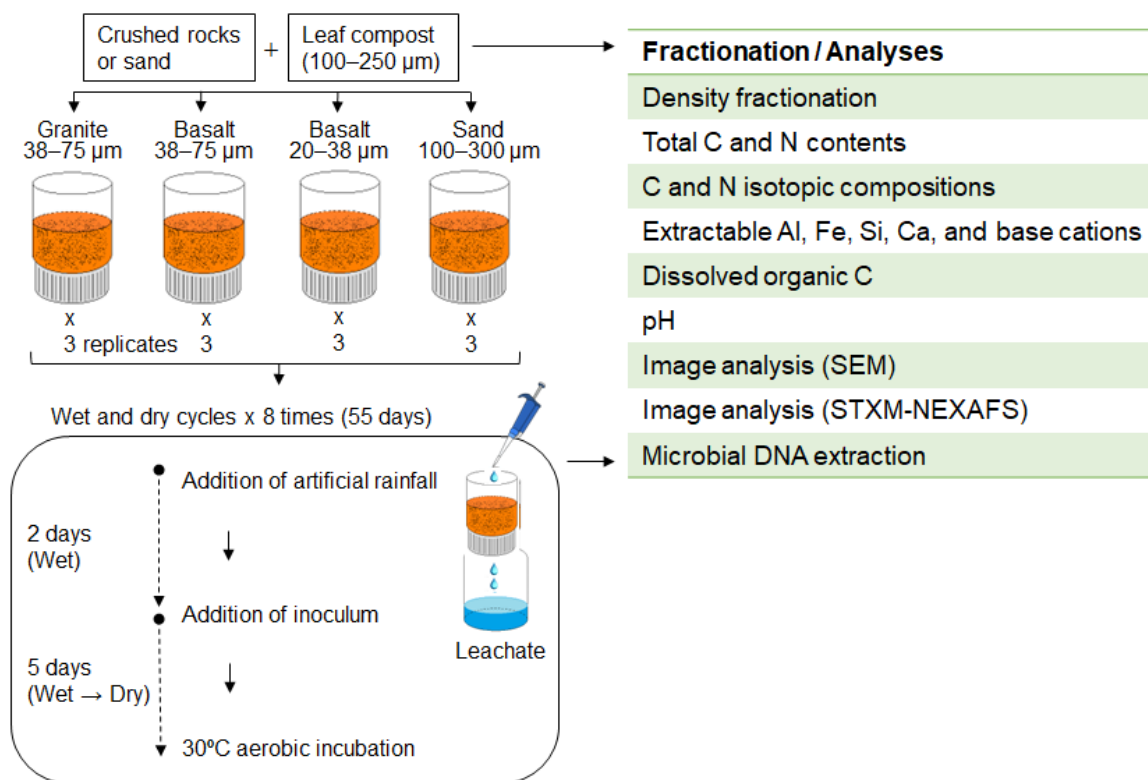


Figure 1. Schematics of the 55-day incubation experiment, including eight wet-and-drywet-dry cycles.

2.1 Source materials and preparation for mineral/rock-organic matter mixture preparations

We selected two rocks with having a contrasting chemical composition and weatherability, and a river sand as a low-reactivity control for comparison this study. Basalt, a mafic igneous rock, weathers faster and releases rock-forming elements including Fe and Al more rapidly than felsic granite due to the difference in silicate mineral composition. In addition to feldspars, basalt comprises minerals of lower degree of consists more of less-polymerization ed/crystalline mineral (e.g., pyroxene) (Halder and Tišljär, 2014), whereas granite consists mainly of more-polymerized is dominated more by high-crystallinity minerals such as (e.g., quartz) and K-feldspar (Gray and Murphy, 2002; Chapman et al., 2009). Granite used in this study was from Hiroshima, Japan ("pan" type, < 75 μm, Yoko Bussan Co.) and Basalt, a mafic igneous rock, dominated by is plagioclase and pyroxene (Halder and Tišljär, 2014), characterized by a higher weathersing rapidly to form rate and faster formation of short-range order (SRO) Fe and Al minerals faster than compared to felsic

150 rocks such as granite which mainly consists of quartz (20–40%), K-feldspar, and Na-plagioclase (Gray and Murphy,
2002; Chapman et al., 2009). Granite from Crushed granite Hiroshima, Japan (“pan” type, $\leq 75 \mu\text{m}$, Yoko Bussan Co. Co.
Ltd., Hiroshima, Japan) used in this study had the elemental and mineralogical composition typical of granite (Table S1,
Fig. S1). Basaltic rock from Akita, Japan (“dust” type, $< 2500 \mu\text{m}$, Horie-Kenzai Co.) used in this study was mainly
155 composed of plagioclase and pyroxene, with minor magnetite, olivine, smectite, and quartz (Fig. S1). The quartz detected
likely resulted from the nearby lithologies. Further characterization of the basaltic rock sample is reported elsewhere
(Yang et al., [under review accepted 2026](#)). This rock is classified as basaltic andesite based on the Total Alkali-Silica
diagram; however, for simplicity, the two particle-size treatments are referred to as “fine” and “coarse basalt”. Granite
used in this study was from Hiroshima, Japan (“pan” type, $\leq 75 \mu\text{m}$, Yoko Bussan Co.) and had the elemental and
mineralogical composition typical of granite (Table S1, Fig. S1).

160 These rocks were sorted for 38–75 μm and, additionally, for 20–38 μm (only basaltic rock). The source granite was
further ground in by a blender (WB-1, Osaka Chemical Co., Ltd., Osaka, Japan); followed by wet sieving to isolate the 38–75
 μm particle-size class. For crushed basalt (“dust” type, $< 2500 \mu\text{m}$, Horie-Kenzai Co. Ltd., Akita, Japan), we prepared two
particle-size classes. Coarse basalt (38–75 μm) was isolated by wet sieving ~~as described above~~. Fine basalt (20–38 μm) was
isolated by repeated sedimentation of $< 38 \mu\text{m}$ materials in deionized water until the supernatant was free of visible particles
165 $< 20 \mu\text{m}$ based on Stokes law. Preferential loss of some fine-grain minerals (e.g., mica) and enrichment of coarser ones (e.g.,
quartz) during the sorting are possible. Mineralogical data, nevertheless, showed the size-sorted materials fall within a
common compositional range (Fig. S1). As a mineral component having the least weatherability, River sand ($93\% \text{SiO}_2$)
with a mean particle size of approximately 100–300 μm (Toyoura Keiseki Kogyo Co., Ltd., Yamaguchi, Japan) served as a
low-reactivity reference was also used in this study. All materials for rocks obtained were oven-dried at 50 °C before mixing
170 with OM.

The mineralogical composition and total elemental compositions of the four rock materials isolated (granite, two
175 sizes of and-basaltic rocks, and sand) were determined by XRD analysis (Fig. S1; MiniFlex600-C, Rigaku
Holdings Corporation, Tokyo, Japan) and X-ray fluorescence analysis (Table S1; NEX CG, Rigaku Holdings
Corporation, Tokyo, Japan, Table S1; Table S1), respectively. Mineralogy of granite and two basaltic rocks was
identified by X-ray diffraction instrument equipped with a Cu tube (MiniFlex600-C, Rigaku, Tokyo, Japan, Fig. S1),
scanned under XRF reduction mode from 3° to 90° (2 θ) with a step size of 0.01°, at a speed of 5° min⁻¹ (basaltic rock) and
10° min⁻¹ (granite). The diffraction patterns were matched to the Crystallography Open Database. Smectite identified may
include vermiculite because no phyllosilicate pre-treatment was applied. The two sizes of basaltic rock used in this study
180 showed similar mineral composition to those reported in Yang et al.; ([under review accepted 2026](#)). were within a common
range for respective rock types. Further characterization of the source basalt is reported elsewhere (Yang et al., [under
review](#)). The total C concentration of the isolated rocks was $< 0.3 \text{ mg g}^{-1}$ (vario MAX cube, Elementar, Germany). Particle
size distributions (LA-920, Horiba Ltd., Kyoto, Japan) confirmed target ranges of the four rock materials (Fig. S2) types,
assessed by a laser scattering particle distribution analyzer (LA-920, Horiba Ltd., Kyoto, Japan), confirmed the target size
185 ranges (Fig. S12). Briefly, the granite (target size: 38–75 μm) had the mean weight diameter (MWD) of 63.9 μm and the
cumulative percentile values (the grain size at which 50% of the grains are coarser, D_{50}) of 55.6 μm (Fig. S1). The coarse
basalt (38–75 μm) had a MWD of 59.8 μm and D_{50} of 52.5 μm . The fine basalt (20–38 μm) had a MWD of 28.8 μm and D_{50}
of 22.9 μm . The sand (100–300 μm) had a MWD of 267.3 μm and D_{50} of 231.6 μm . The specific surface area of the four
190 mineral components (Table S223) was measured by N₂ gas sorption Autosorb iQ (Quantachrome Corp., Boynton Beach, FL,
USA) using a multi-point BET approach (partial pressures of < 0.3) after outgassing under a vacuum at 150 °C. The total C
concentration of the four rock materials was $< 0.3 \text{ mg g}^{-1}$. This trace level of C derived more likely from organic matter
(e.g., dust, microbial debris) rather than inorganic C because, at least for the basaltic rock, calcite was not detected by XRD

and XANES analysis showed no calcite (Yang et al., accepted 2026).

Leaf compost was used as the sole OM source for the mineral-OM mixture/rock-OM mixtures. The compost was produced mainly from tree leaves with composted for one year of composting, was the same material annually applied to the long-term, no-till plus leaf compost management in the experimental field of the Institute for Agro-Environmental Sciences, Tsukuba, Japan (Wagai et al., 2013a). The leaf compost was air-dried, ground, and dry-sieved to a size of 100–250 μm . The compost had a C content of 408 mg g^{-1} with a C:N ratio of 41. The pH of the compost was 5.92 (H_2O) and 5.45 (KCl). The C structure of the compost had carbonyl-C 7.7%, aromatic-C 9.6%, O-alkyl-C 63.3%, and alkyl-C 19.4% (Fig. S23), which was assessed by solid-state ^{13}C nuclear magnetic resonance (NMR) spectrometry using an FT NMR system (JNM-ECA600II, JEOL Ltd., Tokyo, Japan) according to the procedure by Hiradate et al. (2004). The NMR spectrum was divided into chemical shift regions representative of the four major types of C present: 0–45 ppm (alkyl C), 45–110 ppm (O-alkyl C), 110–165 ppm (aromatic C), 165–210 ppm (carbonyl C) (Golchin et al., 1994). The total signal intensity and the proportion contributed by each C type were determined by the integration of the spectral regions.

The rock-OM mixtures were prepared by combining 20.00 g of each rock material. The fine and coarse basalt, granite, coarse and fine basalt, and river sand (20.00 g each) were well mixed with 2.50 g of the leaf compost under dry conditions in three replicates (Table S334). The mineral-OM mixture/rock-OM mixtures prepared had an initial C content of 4.5%, comparable to C-rich which is the higher end of the C level for cultivated topsoils. For the incubation experiment, the mixtures were placed then transferred into a 50 mL plastic columns fitted with two the bottom covered with double layers of nylon mesh (sheet (\approx approximately 6 μm -mesh) at the bottom size) (Fig. 1).

2.2 Aerobic incubation with and repeated leaching with wet/dry cycles

The mineral-OM mixture/rock-OM mixtures were subjected to weekly repeated leached weekly ing events with using artificial rainwater over a 55-day experimental period/duration. The artificial rainwater composition was prepared to represent typical a common Japanese precipitation chemical composition of rainwater in Japan based on the typical Japanese precipitation data from the national acid deposition survey in 2014 (Horie et al., 2016): The pH chemical composition of rainwater was pH of 4.73 and contained the following ionic concentrations: SO_4^{2-} 18.1 $\mu\text{mol L}^{-1}$; NO_3^- 15.4 $\mu\text{mol L}^{-1}$; Cl^- 90.2 $\mu\text{mol L}^{-1}$; NH_4^+ 17.9 $\mu\text{mol L}^{-1}$; Na^+ 76.6 $\mu\text{mol L}^{-1}$; K^+ 2.62 $\mu\text{mol L}^{-1}$; Ca^{2+} 5.37 $\mu\text{mol L}^{-1}$; and Mg^{2+} 9.04 $\mu\text{mol L}^{-1}$. The solution was prepared using analytical-grade reagents: we used reagents of HCl, KCl, CaCl_2 , $\text{MgSO}_4 \cdot 7\text{H}_2\text{O}$, NaNO_3 , $(\text{NH}_4)_2\text{SO}_4$, and NaCl.

The microbial inoculum was prepared from 0–5 cm the well characterized surface soil (0–5 cm) off from a the long-term experimental field under (no-till management with annual leaf compost input at the Institute for Agro-Environmental Sciences, Tsukuba, Japan (Wagai et al., 2013a). plot, where was the same leaf compost served material as the sole organic matter/OM source for the rock-OM mixtures annually applied to the long-term, no-till plus leaf compost management in the experimental field of the Institute for Agro-Environmental Sciences, Tsukuba, Japan (Wagai et al., 2013a); see above). The soil is classified as a Hydric Hapludand (Soil Survey Staff, 2014) and a Hydric-Silic Andosol (IUSS Working Group WRB, 2015). The microbial inoculum was produced/obtained by mixing the field-moist soil with deionized water (1:15, w/v) at a ratio of 1:15, and shaking the suspension the mixture was shaken for 30 min with glass beads for 30 min. After that, the mixture was then filtered through a 5- μm membrane filter (slightly modified from Wagai and Sollins, 2002) to retain/keep bacteria and fungal spores/fragments in suspension while removing major grazers. The inoculum was stored at 4 $^\circ\text{C}$ for no longer than in a refrigerator for no more than 24 h before use/inoculation events.

The incubation started with was initiated by gently applying 40 mL of artificial rainwater applied to each column, from the surface. The column was left at room temperature overnight, and the leachate was collected. This weekly e volume of rainwater added every 7 days corresponded was roughly equal to Japan's the mean average annual precipitation of Japan, assuming an even rainfall distribution of rainfall events over a year (Horie et al., 2016). After leachate collection

235 the leachate, 1 mL of microbial inoculum was added to each column. The water content of the mineral-OM mixture/rock-
OM mixtures at this point was 52–63% on an air-dried basis (Table S445). The CCAH columns were then incubated in the
dark at 30 °C for 5 days until, which made nearly complete drying, forming the water content nearly zero. The rock-OM
240 mixtures became partially cemented material during each drying cycle. Before the subsequent wetting each time phase, the
hardened material in each column was gently loosened with a spatula to approximately half the column depth to facilitate
infiltration of rainwater and inoculum by inserting a spatula to approximately half the column depth to facilitate the diffusion
of rainwater and microbial inoculum into the mixture. The clod formed in the column was then physically mixed into small
pieces using a spatula. Subsequent wet and dry cycles received was initiated by applying 40 mL of rainwater
and again, followed by 0.1 mL of inoculum (reduced from instead of 1 mL of inoculum added the first cycle time).
Eight wet-dry cycles were completed in was repeated eight times over the 55-day incubation duration (Fig. 1). After
245 incubation, the mineral-OM mixture/rock-OM mixtures after the incubation (Table S34) were gently
disaggregated/homogenized into small pieces, and sieved (sieved through a 2-mm mesh using a spatula, and homogenized
thoroughly mixed in a plastic bag, and split for further analysis, except for microbial analyses using meso-density
fraction under wet conditions (Table S565). The leachates collected after each wet and dry cycle from each column were
combined for each replicate and to analyze before filtration for the concentrations of analyses of dissolved organic C
250 (DOC), Al, Fe, Si, and base cations (Na, Ca, K, and Mg), and well as pH.

2.3 Density fractionation before and after the incubation

The mineral-OM mixture/rock-OM mixtures after the incubation were fractionated by density with a moderate dispersion by
mechanical shaking to distinguish organo-mineral assemblages as a meso-density fraction (1.8–2.4 g cm⁻³; MF) from
particulate OM as a low-density fraction (< 1.8 g cm⁻³; LF) and crushed rock as a high-density fraction (> 2.4 g cm⁻³; HF)
255 using sodium polytungstate (SPT 0 grade, TC Tungsten Compounds GmbH, D-96271 Grub am Forst, Germany), as
described in Wagai et al. (2015). For the pre-incubation samples, crushed rocks and sand were fractionated by density to
distinguish MF (< 2.4 g cm⁻³) the fraction (< 2.4 g cm⁻³) and HF (> 2.4 g cm⁻³). The initial leaf compost is regarded as
LF, so that the theoretical bulk value in the mixture, including each mineral component and the leaf compost on Day 0, is
calculated using each component's data. Briefly, the initial crushed rocks (4.0 g) as the pre incubation samples or 10.0 g of
260 the mineral-OM mixture/rock-OM mixture after the incubation were mixed with 30 mL of sodium polytungstate (SPT-0
grade, TC-Tungsten Compounds GmbH, D-96271 Grub am Forst, Germany) with a final density of 1.8 g cm⁻³ and shaken at
120 rpm for 30 min. The suspension was then centrifuged at 2330 g for 20 min, and the floating material was collected on a
0.45 µm membrane filter. These steps were repeated at least three times to maximize the recovery. The material on the filter
was washed with deionized water until the electric conductivity was below 50 mS cm⁻¹; this operation produced the LF
265 fraction. The residue was resuspended in SPT solution adjusted to 2.4 g cm⁻³ at the sample: extractant ratio of 10 g:30 mL,
shaken, and centrifuged. The floating material (1.8–2.4 g cm⁻³) was transferred to a 250 mL centrifuge bottle, mixed with
deionized water, and centrifuged at 17,000 g for 20 min. The supernatant was decanted, and this rinsing step was repeated
until the electric conductivity of the supernatant became < 50 mS cm⁻¹. The final material was recovered as the MF fraction
of 1.8–2.4 g cm⁻³. The remaining residue (> 2.4 g cm⁻³) was rinsed with deionized water in the same way as above to isolate
270 the HF fraction of > 2.4 g cm⁻³. Recovered LF was oven-dried at 80 °C, and MF and HF were freeze-dried. Masses
recovered in each density fraction from the rock-OM mixtures on Day 0 and Day 55 are shown in Table S67. The materials
recovered in MF by this operation are, therefore, organo-mineral aggregates that are physically resistant to the disruptive
forces from the fractionation steps (esp. repeated mechanical shaking).

The initial four rock materials were fractionated at a density of at 2.4 g cm⁻³ to distinguish MF and HF. Assuming that the
275 initial leaf compost entirely consists of LF, we calculated C, N, and extractable Al, Fe, Si levels in each fraction for the rock-
OM mixtures on Day 0. Masses recovered in each density fraction from the rock-OM mixtures on Day 0 and Day 55 are

[shown in Table S6.](#)

2.4 Chemical analyses of the mixtures

Total C and N contents in the density fraction were determined by an elemental analyzer (vario MAX cube, Elementar Analysensysteme GmbH, Langenselbold, Germany). [The degree of microbial alteration of OM can be assessed by C and N isotopic compositions \(e.g., Sollins et al., 2009\).](#) Thus, [initial leaf compost and density fractions under the two basalt treatments after the incubation were analyzed by](#) ~~The C and N isotopic compositions of the initial leaf compost and the density fractions under the two basalt treatments after the incubation were analyzed on the~~ a continuous-flow stable isotope mass spectrometer (Delta V Advantage, Thermo Fisher Scientific Inc., USA) coupled with an elemental analyzer (Flash EA 1112 Series). To minimize the N blank, a gas-tight automatic sampler was used (Zero Blank Autosampler, Costech Analytical Technologies Inc., USA). To increase the sensitivity for analyzing the N isotopes, the combustion and reduction tubes (both 18 mm outer diameters) were exchanged with thinner ones (18–10 mm and 10–6 mm outer diameters, respectively; Ogawa et al., 2010; Koba et al., 2021). The obtained $^{13}\text{C}/^{12}\text{C}$ and $^{15}\text{N}/^{14}\text{N}$ ratios are shown in terms of the δ value ($\delta^{13}\text{C}$ and $\delta^{15}\text{N}$) relative to Vienna Pee Dee Belemnite and the air dinitrogen, respectively. Their analytical precisions are $\pm 0.2\%$ except for the $\delta^{15}\text{N}$ values of the HF ($\pm 0.4\%$).

Extractable Al, Fe, Si, and Ca in the density fraction and bulk samples were quantified by the sequential extraction with sodium pyrophosphate (PP), oxalate-extractable (OX), and dithionite-extractable (DC), as described in Wagai et al. (2018). These extractions have been widely used as a practical method to estimate the concentrations of organo-metal complexes, short-range-ordered minerals, and pedogenic Fe oxides, respectively (Shang and Tiessen, 1998; Heckman et al., 2018; Ashida et al., 2021; Hall and Thompson, 2022). However, cautions are required for their interpretation due to the limited selectivity in extracting target phases as discussed previously (Wagai et al., 2013b; Rennert, 2019; Fukumasu et al., 2025). Briefly, each sample was extracted with 0.1 M sodium pyrophosphate (pH 10) at a sample: extractant ratio of 0.1 g:10 mL at 120 rpm for 16 h at room temperature, followed by high-speed centrifugation at 29,000 g for 40 min. After collecting an aliquot of the extract (approximately 7 mL) and discarding the remaining supernatant, the residue was extracted with 10 mL of 0.2 M acidified sodium oxalate solution (pH 3) at 150 rpm for 4 h at 25 °C in the dark and centrifuged in the same way. After collecting an aliquot of the extract and discarding the remaining supernatant, the residue was added 0.167 g of sodium dithionite and then extracted with 10 mL of 0.646 M sodium citrate at 120 rpm for 16 h at room temperature and centrifuged in the same way.

The amounts of Al, Fe, Si, and base cations (Na, Ca, K, and Mg) after each of the three extractions were measured by an inductively coupled plasma optical emission spectrometer (700 series ICP-OES, Agilent Technologies, Inc., CA, United States). The combined leachate from the eight ~~wet-and-dry~~ [wet-dry](#) cycles ~~for~~ [from](#) each column [of all four treatments](#) was also analyzed in the same way. The leachate was also analyzed for DOC by a TOC analyzer (TOC-L, Shimadzu, Kyoto, Japan) using non-permeable organic C mode and for pH.

The pH of the bulk samples [from all four treatments](#) after the incubation was measured using a glass electrode in ultra-pure water (0.4 g: 4 mL) after 1 h of shaking at 150 rpm. Subsequently, we added 1.6 mL of 3.5 M KCl to the water suspension to measure pH in the 1 M KCl conditions.

2.5 Imaging analyses of selected samples

Microscopic observation of the initial crushed rocks (granite, coarse basalt, and fine basalt) as well as the MF of their mixtures after the incubation was done using a scanning electron microscope (SU1510, Hitachi High-Tech Corporation, Tokyo, Japan). The subsets of MFs (stored in a suspension at ca 5 °C after the density fractionation without freeze-drying) were diluted in ultra-pure water and deposited on a carbon tape, air-dried, and coated with palladium before the observation.

[The subsets of MF from selected treatments \(granite and coarse basalt\) were assessed to examine the spatial arrangement](#)

of C, Al, and Fe, as well as C functional group within the meso-density materials (largely present as shaking-resistant microaggregates) in MF using scanning transmission X-ray microscopy (STXM) and near-edge X-ray absorption fine structure (NEXAFS). Another subset of suspended MF (The subsets of MF from selected treatments (granite and coarse basalt) using scanning transmission X-ray microscopy (STXM) and near-edge X-ray absorption fine structure (NEXAFS) to assess to examine the spatial arrangement of key elements (C, Al, and Fe) and C structure within the meso-density materials (largely present as shaking-resistant microaggregates) present in MF. Another subsets of MF in suspension were diluted with ultra-pure water and weakly sonicated ($< 10 \text{ J mL}^{-1}$) followed by deposition on a Si_3N_4 window (50 nm thick, window size 500 μm). To minimize the re-aggregation on the Si_3N_4 window upon drying, the samples were slowly dried at room temperature. Carbon, Al, and Fe were recorded by a compact STXM at BL-19A beamline in the Photon Factory of the High Energy Accelerator Research Organization, Ibaraki, Japan (Takeichi et al., 2016). The STXM data analysis was carried out with the IDL package aXis 2000 (Hitchcock, 2023). The distribution maps of C, Al, and Fe were obtained by subtracting the post-edge optical density (OD) image from the pre-edge OD image, respectively. Specifically, we collected images in the X-ray energy region of 280.0 and 300.0 eV for C K-edge adsorption, 700 and 709.5 eV for Fe L-edge adsorption, and 1550.0 and 1567.0 eV for Al K-edge adsorption (Solomon et al., 2012). The spatial resolution of the images was 200 nm. Deposited materials inevitably have sample thickness variation. Interpretation of the spectral results therefore requires cautions because the obtained signal from each pixel is intensified in the thicker region of the deposited sample (Wan et al., 2007).

2.6 Microbial community analyses

Bacteria may likely exert stronger control effect on rock weathering than fungi under our short-term conditions with repeated physical mixing. We thus We also assessed the changes in bacterial community 16S amplicon sequencing using the initial leaf compost ($n = 3$, air-dry conditions), bulk samples from all four treatments on Day 55 ($n = 3$, air-dry conditions), and MF from selected treatments (granite, coarse basalt, and fine basalt) on Day 55 ($n = 1$, wet conditions) after the incubation. The latter was a composite of three reps due to the limited mass recovery of MF. The DNA was extracted from 0.4 g of each sample under wet conditions by the the-FastDNA® SPIN Kit for Soil (MP Biomedicals, California, USA) according to the manufacturer's instructions with a few modifications. Quantitative PCR (qPCR) assays were conducted using the fluorescent dye SYBR Green (THUNDERBIRD Next SYBR qPCR mix, Toyobo OYOB) by a QuantStudio 3.0 real-time PCR System (Applied Biosystems/Thermo Fisher Scientific). 16S rRNA genes quantified using the primer pairs Bact1369F/ProK1492R (Suzuki et al., 2000) for the V3-V4 region of the 16S rRNA. The PCR reactions for 16S rRNA started with an initial denaturing step at 95 °C for 30 s, followed by 40 cycles at 95 °C for 5 s and 60 °C for 30 s. Melting curve analyses involved a denaturing step at 95 °C for 15 s, annealing at 65 °C for 1 min, and melting in 0.1 °C steps up to 95 °C. Standard curves for each assay were generated by serial dilutions of linearized plasmids with cloned fragments of environmental DNA. Amplification efficiencies were 96.4 %. 16S rRNA amplicon sequencing and subsequent bioinformatics analysis are the same as the previous studies (Bamba et al., 2024; Hara et al., 2024). DNA sequencing data (16S rRNA gene amplicon) are available at the NCBI Sequence Read Archive (SRA) under BioProject ID PRJDB18777. For the 16S rRNA amplicon, taxonomy was assigned to ASVs using the SINTAX algorithm (Edgar, 2016) implemented in USEARCH (v11.0.667) against the RDP database v18 (Cole et al., 2014).

2.7 Statistics and calculations

The effects of rock treatment mineral type on the measured variables were tested by one-way ANOVA, followed by a Tukey's post hoc test. The changes in the variables before and after over the incubation were evaluated duration were examined by using paired t -tests. All statistical analyses were performed in Microsoft Excel for Microsoft 365 MSO and Excel Toukei (BellCurve for Excel, Social Survey Research Information, Tokyo, Japan).

We estimated the total amounts of extractable metals in the rock-OM mixtures after the incubation by summing up the

metals in LF, MF, and HF instead of the bulk sample values because we expected less sub-sampling error from the former. Specifically, roughly 44% of the mass of the incubated mixture was used for the density fractionation analysis, whereas only 13% was allocated for bulk sample chemistry. The high mass recovery of the density fractions (range: 99–101%, Table 1) suggests that this approach was appropriate. C and N in the mineral-OM mixtures after the incubation by summing up the C and N in LF, MF, and HF instead of the bulk sample values because we expected less sub-sampling error from the former. Specifically, roughly 44% of the mass of the incubated mixture was used for the density fractionation analysis, whereas only 13% was allocated for bulk sample C and N analysis. We estimated the total amounts of the extractable metals in the same way. The high mass recovery of the density fractions (range: 99–101%, Table 1) suggests that justified this approach was appropriate.

Table 1. Recovery of mass, C, N, and extractable Al, Fe, and Si after the density fractionation of the mineral-OM mixture/rock-OM mixtures on Day 55.

	Mass (%)		C (%)		N (%)		Extractable Al (%)		Extractable Fe (%)		Extractable Si (%)	
Granite 38–75 μm	±	±	9	±	±	±	N.A.		N.A.		N.A.	
	0	±	5	±	0	±	N.A.		N.A.		N.A.	
	0	±	5	±	0	±	N.A.		N.A.		N.A.	
Basalt 38–75 μm	9	±	8	±	9	±	8	±	9	±	8	±
	9	±	6	±	0	±	8	±	9	±	5	±
	9	±	6	±	0	±	8	±	9	±	5	±
Basalt 20–38 μm	±	±	±	±	±	±	9	±	±	±	9	±
	0	±	0	±	0	±	5	±	0	±	3	±
	0	±	2	±	6	±	5	±	8	±	3	±
Sand 100–300 μm	±	±	±	±	±	±	N.A.		N.A.		N.A.	
	0	±	0	±	0	±	N.A.		N.A.		N.A.	
	±	±	7	±	9	±	N.A.		N.A.		N.A.	

Al and Fe were extracted sequentially with sodium pyrophosphate, acid oxalate, and dithionite-citrate.

Value shows mean ± standard deviation ($n = 3$).

N.A.: Not analyzed due to limited mass recovery of MF meso-density fraction.

Alpha and beta diversities of the bacterial communities in the initial leaf compost and post-incubation samples were calculated using the “phyloseq” pipeline (McMurdie and Holmes, 2013) and the “microeco” pipeline (Liu et al., 2021), respectively. Principal coordinate analysis (PCoA) of unweighted UniFrac distance was used to visualize beta diversity between the treatments. We estimated the influence of the mineral type in the mineral-OM mixture/rock-OM mixtures on the beta diversity by permutational multivariate analysis of variance (PERMANOVA) using the ‘adonis’ function in the ‘vegan’ package (Oksanen, 2013). We further analyzed the correlations between the bacterial composition and the property variables of MF and bulk samples on Day 55 and initial compost by the Mantel test using the ‘mantel’ function in the ‘ecodist’ package (Goslee and Urban, 2007). All the microbial analyses were performed using R version 4.2.0 (www.r-project.org).

We presented and discussed the mass, C and N, and extractable metal data of bulk and density fractions in multiple ways (e.g., per fraction vs. per bulk mass basis). Tables and figures of these data are summarized in Table S7.

3 Results

3.1 Recovery after density fractionation

Density fractionation of the mineral-OM mixture/rock-OM mixtures at the end of the 55-day incubation experiment showed reasonable recoveries for all the mineral treatment/rock treatments: 99–101% for mass, 86–107% for C, 90–109% for N, 88–

390 95% for extractable Al, 99–108% for extractable Fe, and 85–93% for extractable Si (Table 1). [Metal recovery data is not available for granite and sand treatment as the metal extraction of LF and MF was not possible due to the limited mass.](#) Some variations among the [mineral treatment/rock treatments](#) were found. The coarse basalt treatment had less complete C and N recoveries than the other treatments and less complete extractable Al and Si recoveries relative to the fine basalt treatment. Overall, we considered that these recoveries were at acceptable levels for further assessment of the elemental distribution patterns across the density fractions.

395

Table 1. Recovery of mass, C, N, and extractable Al, Fe, and Si after the density fractionation of the rock-OM mixtures on Day 55.

	Mass (%)	C (%)	N (%)	Extractable Al (%)	Extractable Fe (%)	Extractable Si (%)
Granite 38–75 μm	100 \pm <1	95 \pm 12	100 \pm 6	N.A.	N.A.	N.A.
Basalt 38–75 μm	99 \pm 1	86 \pm 8	90 \pm 8	88 \pm 7	99 \pm 6	85 \pm 3
Basalt 20–38 μm	100 \pm <1	102 \pm 1	106 \pm 1	95 \pm 3	108 \pm 1	93 \pm <1
Sand 100–300 μm	101 \pm <1	107 \pm 14	109 \pm 18	N.A.	N.A.	N.A.

[Al, Fe, and Si were extracted sequentially with sodium pyrophosphate, acid oxalate, and dithionite-citrate reagents.](#)

[Value shows mean \$\pm\$ standard deviation \(\$n = 3\$ \).](#)

400 [N.A. Not analyzed due to the limited mass recovery of the meso-density fraction. Al and Fe were extracted sequentially with sodium pyrophosphate, acid oxalate, and dithionite citrate.](#)

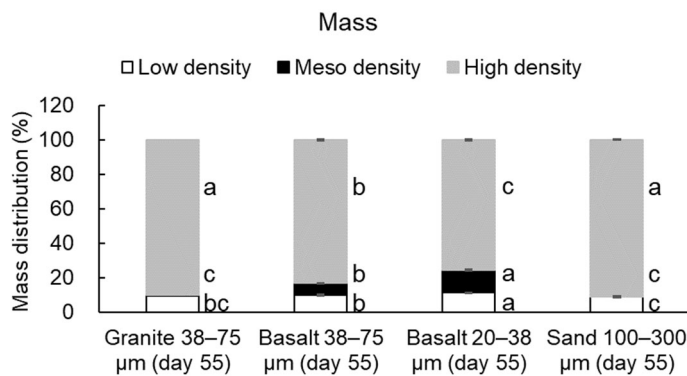
[Value shows mean \$\pm\$ standard deviation \(\$n = 3\$ \).](#)

[N.A. Not analyzed due to limited mass recovery of meso-density fraction.](#)

405 3.2 Mass, C and N, and $\delta^{13}\text{C}$ and $\delta^{15}\text{N}$

Mass proportion in MF after the incubation was the highest in the fine basalt (13%), followed by the coarse basalt (7.1%), granite (0.57%), and sand (0.17%) treatments (Fig. 2). The increases in MF largely corresponded to the reduction in the mass of HF. However, the initial granite, coarse basalt, and fine basalt contained small amounts of MF, accounting for 0.30%, 6.8%, and 6.3% of the initial mass of respective minerals (Fig. 3a). After accounting for the initial MF in these treatments,

410 we detected a significant increase in the mass of MF after the incubation for the granite and fine basalt treatments (Fig. 3a). The largest increase in MF mass was found in the fine basalt treatment (65 mg g^{-1} bulk) whereas that in the coarse basalt and sand treatments changed little (0.26–3.0 mg g^{-1} bulk) over the 55-day duration.



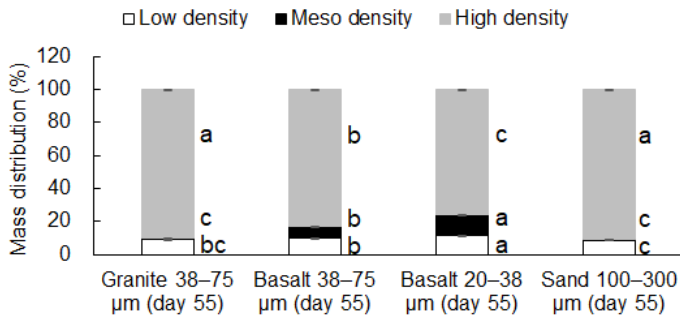


Figure 2. Mass distributions of the four mineral-OM mixtures across low-, meso-, and high-density fractions on Day 55. For the same letters in each density fraction (i.e., low-, meso-, or high-density), significant differences among the four rock treatments were shown by different letters; are not significantly different at $P < 0.05$ (Tukey's test; $n = 3$).

The C concentration in LF on Day 0, the initial leaf compost on Day 0, was 408 mg g^{-1} fraction (Table S8-1), whereas that on Day 55 ranged from 378 to 431 mg g^{-1} fraction (data not shown Table S899-1) in comparison with the initial leaf compost (408 mg C g^{-1}). Carbon distribution in LF-The C distribution to LF differed among the treatments in the following order: fine basalt > coarse basalt > granite > sand (Table S489-2). The same pattern was found for MF and HF. Because the initial crushed mineral crushed rocks contained only small amounts of MF mass (Fig. 3a, Table S6) that had only trace level of and essentially no C (Fig. 3b; Table S78-1, S78-2), the C increase in MF after the incubation was significant for all four treatments ($P < 0.01$, Fig. 3b). The largest increase was shown in the fine basalt (1.50 ± 0.051 to 31.3 mg C g^{-1} bulk) followed by the coarse basalt (1.03 ± 0.070 to 90.93 mg C g^{-1} bulk) and then the granite (0.60 ± 0.060 to 550.55 mg C g^{-1} bulk) treatments. Even in the sand treatment, we detected a significant increase in the amount of C in MF (0.100 to 100.10 ± 0.01 mg C g^{-1} bulk). When summing up the C and N in all three fractions, the total amounts of C and N left after the incubation showed a significant difference among the treatments in the following order: fine basalt > coarse basalt > granite > sand (Table S489-2).

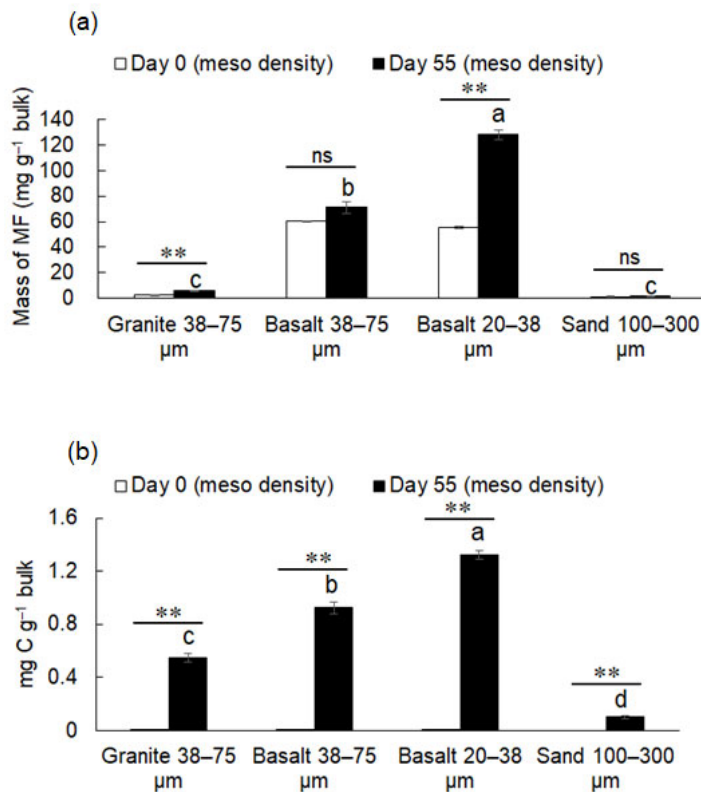


Figure 3. The mass of meso-density fraction (MF) in the mineral-OM mixture/rock-OM mixtures before (Day 0) and after the incubation (Day 55) (a). The amounts of C in MF in the bulk mixtures on Day 0 and Day 55 (b). For the Day 0 samples, the initial s were fractionated by density to distinguish MF and HF. Initial leaf compost is regarded as LF, so that the theoretical bulk value in the mixture on Day 0 is calculated using each component's data. Significant differences among the rock treatments on the same day are shown by different letters at $P < 0.05$ (Tukey's test; $n = 3$). The increase in MF from Day 0 to Day 55 is shown with asterisks (** in the meso-density fraction "on Day 55" or "on Day 0" in each experimental day are not significantly different at $P < 0.05$ (Tukey's test; $n = 3$). Differences between the meso-density fraction "on Day 0" and "on Day 55" in each in MF are significant at $**P < 0.01$; ns, not significant (t test).

The C:N ratio of the initial leaf compost and that of LF after the incubation were similar in all four treatments (Fig. 4a, Table S9-1); because the majority of C was present in LF. When comparing the density fractions, the C:N ratio progressively declined with increasing density. In other words, more C was lost relative to N of OM from LF towards HF during the incubation was greater for C than N (Table S489). The isotopic values (of $\delta^{13}\text{C}$ and $\delta^{15}\text{N}$) of the initial leaf compost and those of LF after the incubation were similar in both basalt treatments (Fig. 4b, 4c). The value of $\delta^{13}\text{C}$ significantly increased from LF towards HF, whereas $\delta^{15}\text{N}$ showed a significant increase from LF to MF and a slight apparent decline from MF to HF (Fig. 4b, 4c).

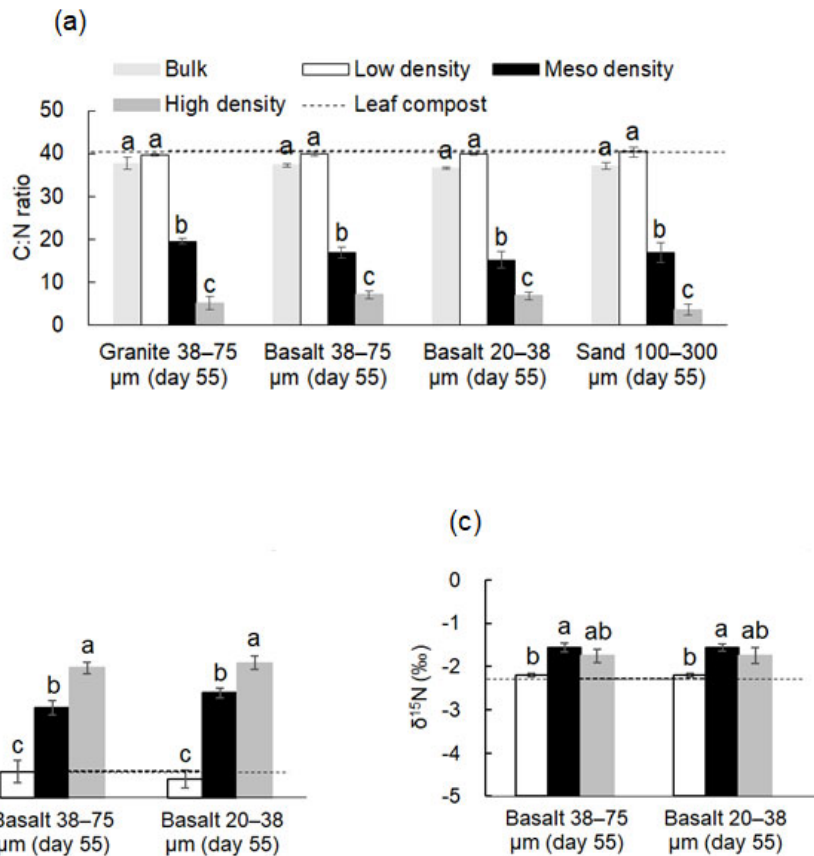


Figure 4. C:N ratio (a), $\delta^{13}\text{C}$ (b), and $\delta^{15}\text{N}$ (c) among the density fractions from gradient in the four rock treatments mineral-OM mixtures on Day 55 (a) and those of initial leaf compost as a horizontal dotted line. No $\delta^{13}\text{C}$ and $\delta^{15}\text{N}$ analyses were done for granite and sand treatment due to the limited mass of MF, and values of $\delta^{13}\text{C}$ and $\delta^{15}\text{N}$ along density gradient of the two basalt treatments on Day 55. Significant differences among the density fractions are shown with letters and in the leaf compost (b). The same letters in each bulk or each density fraction (i.e., low-, meso-, or high-density) among the s are not significantly different letters at $P < 0.05$ (Tukey's test; $n = 3$; a). The same letters in each among each density fraction (i.e., low-, meso-, or high-density) are not significantly different at $P < 0.05$ (Tukey's test; $n = 3$; b).

3.3 Extractable Al, Fe, and Si and pH

The initial sand contained only negligible amounts of OX-extractable metals (metal_{OX}), and the initial granite contained $< 1 \text{ mg g}^{-1}$ bulk of metal_{OX} (Table S23), whereas the initial coarse and fine basalts contained had much greater higher extractable metals (Table S2). Particularly, the initial fine basalt had a higher amount of PP-extractable Al, Fe, and Si (Al_{PP} , Fe_{PP} , Si_{PP}) as well as Al_{OX} , Fe_{OX} , and Si_{OX} compared to the initial coarse basalt. The higher extractable Al and Fe in the fine basalt may be explained in part by the slightly higher total contents of these metals, but that was not the case for Si (Table S12).

After the 55-day incubation, we detected some increases in the metal concentrations extractable metals in LF consistently and in the MF increased for from Fe_{OX} , Fe_{DC} , Fe_{PP} , and Al_{PP} among the four rock treatments, but especially for the basalt treatments the two basalt treatments (Table 2; Table S5910-1; Table S5910-2; Table S61011;), where we were able to recover enough masses of MF (Fig. 2; Table S67). For the basalt treatments where enough MF No extraction from MF was possible for the granite and sand treatments due to the very low mass recovery allowed the metal extractions (Fig. 2; Table S67), a major increase in metal concentration was shown in Fe_{OX} , Al_{OX} , Si_{DC} , and Al_{PP} for fine basalt, and Si_{DC} and Al_{PP} for coarse basalt. In HF, major changes were the decline in Fe_{OX} and Al_{OX} concentration for coarse basalt (Table 2; Table S10-1).

Table 2. Concentrations (mg g⁻¹ per fraction) of Al, Fe, and Si dissolved by sequential extractions in each density fraction from the rock-OM mixtures on Day 55.

	Sodium pyrophosphate (PP)			Acid oxalate (OX)			Dithionite-citrate (DC)			Total		
	Al	Fe	Si	Al	Fe	Si	Al	Fe	Si	Al	Fe	Si
<i>Low-density fraction (< 1.8 g cm⁻³)</i>												
Granite 38–75 μm	0.33 ± 0.03	0.25 ± <0.01	3.0 ± 0.1	1.0 ± <0.1	1.7 ± <0.1	0.51 ± 0.01	0.30 ± 0.03	1.5 ± 0.1	2.7 ± 0.2	1.6 ± 0.1	3.4 ± 0.1	6.2 ± 0.3
Basalt 38–75 μm	0.48 ± 0.01	0.53 ± 0.02	2.0 ± 0.1	1.4 ± 0.1	3.3 ± 0.1	0.67 ± 0.02	0.37 ± 0.01	2.1 ± <0.1	4.0 ± 0.1	2.2 ± 0.1	5.9 ± 0.1	6.6 ± 0.1
Basalt 20–38 μm	0.52 ± 0.02	0.71 ± 0.02	1.6 ± <0.1	2.0 ± 0.1	6.3 ± 0.1	1.2 ± <0.1	0.48 ± 0.01	3.3 ± 0.1	6.4 ± 0.1	3.0 ± <0.1	10 ± <1	9.2 ± 0.1
Sand 100–300 μm	0.39 ± 0.01	0.24 ± <0.01	3.1 ± 0.2	1.1 ± 0.1	1.6 ± <0.1	0.49 ± 0.03	0.26 ± 0.04	1.1 ± 0.1	2.4 ± 0.3	1.7 ± 0.1	3.0 ± 0.1	6.0 ± 0.4
<i>Meso-density fraction (1.8–2.4 g cm⁻³)</i>												
Granite 38–75 μm	N.A.	N.A.	N.A.	N.A.	N.A.	N.A.	N.A.	N.A.	N.A.	N.A.	N.A.	N.A.
Basalt 38–75 μm	0.44 ± 0.01	0.76 ± 0.04	1.7 ± <0.1	13 ± 3	51 ± 11	6.1 ± 1.3	2.7 ± 0.1	16 ± 1	9.6 ± 0.2	17 ± 3	68 ± 11	17 ± 1
Basalt 20–38 μm	0.44 ± <0.01	0.69 ± 0.02	1.7 ± <0.1	18 ± 1	74 ± 1	9.4 ± 0.2	2.4 ± 0.1	14 ± <1	9.2 ± 0.1	21 ± 1	89 ± 1	20 ± <1
Sand 100–300 μm	N.A.	N.A.	N.A.	N.A.	N.A.	N.A.	N.A.	N.A.	N.A.	N.A.	N.A.	N.A.
<i>High-density fraction (> 2.4 g cm⁻³)</i>												
Granite 38–75 μm	0.0 ± <0.1	0.0 ± <0.1	0.0 ± <0.1	0.12 ± 0.02	0.68 ± 0.04	0.13 ± 0.02	0.18 ± 0.01	1.8 ± 0.0	0.73 ± 0.02	0.30 ± 0.03	2.5 ± 0.1	0.86 ± 0.04
Basalt 38–75 μm	0.071 ± 0.011	0.23 ± 0.01	0.36 ± 0.02	3.7 ± 0.1	25 ± 1	2.2 ± 0.1	0.72 ± 0.04	4.8 ± 0.3	8.9 ± 0.2	4.5 ± 0.1	30 ± 1	11 ± <1
Basalt 20–38 μm	0.15 ± <0.01	0.28 ± <0.01	0.57 ± 0.02	4.7 ± 0.1	34 ± 1	3.1 ± <0.1	0.59 ± 0.05	4.9 ± 0.6	9.2 ± 0.1	5.4 ± 0.1	39 ± 1	13 ± <1
Sand 100–300 μm	0.0 ± <0.1	0.0 ± <0.1	0.0 ± <0.1	0.015 ± 0.008	0.14 ± 0.10	0.0 ± <0.1	0.087 ± 0.014	1.3 ± 0.3	0.080 ± 0.021	0.10 ± 0.01	1.4 ± 0.4	0.080 ± 0.021

Al, Fe, and Si were extracted sequentially with sodium pyrophosphate, acid oxalate, and dithionite-citrate reagents.

Value shows mean ± standard deviation (n = 3).

N.A. Not analyzed due to the limited mass recovery of the meso-density fraction.

Concentrations (per fraction) on Day 0 are represented in Table S10-1. Al, Fe, and Si were extracted sequentially with sodium pyrophosphate, acid oxalate, and dithionite-citrate reagents.

Value shows mean ± standard deviation (n = 3).

N.A. Not analyzed due to limited mass recovery of meso-density fraction.

The distribution of these metal phases across the density fractions, accounting for their masses, showed that the initial rock-OM mixtures held most of the extractable metal phases in HF (Table S10-2) and that the incubation led to enrichment of Fe, Al, Si, especially oxalate-extractable phases, in MF for the two basalt treatments (Table S11). Overall, the distribution of total extractable Fe in MF changed from 11-12% to 16-27% of the respective bulk samples (i.e., LF+MF+HF at Day 0 and 55) (Table S10-2, S11). Similarly, total extractable Al also increased from 15-19% to 23-38% and Si showed a similar pattern. Among the three extractions, major increases over the incubation occurred in the Fe_{OX}, Al_{OX}, and Si_{OX} phases in MF particularly for fine basalt treatment, which was in part balanced by their decreases in HF (Table S10-2, S11). Similar but weaker trends were shown for Fe_{DC}, Al_{DC}, and Si_{DC} phases, while the changes in pyrophosphate-extractable phases remain minor. On a bulk sample basis, total extractable Fe in MF increased from 3.63-9.424.5 to 4.95.4-11.43 mg g⁻¹ and Al from 0.881.1-1.01.2 to 1.21.4-2.73.1 mg g⁻¹ during the incubation. Concurrently, the total extractable Fe in HF slightly decreased from 28–30 to 25–29 mg g⁻¹ and Al from 4.2–4.9 to 3.7–4.1 mg g⁻¹ during the incubation. These changes mainly occurred in oxalate-extractable phases: Al_{OX} and Fe_{OX} in MF after the incubation accounted for 82–89.87% and 76–86.83% of the total extractable metal pools, respectively (Table S11). As a result, MF showed statistically detectable increases (thus accumulation) of Al, Fe, and Si, especially, in OX-extractable pools, for fine basalt (Fig. 5a-c), whereas a small but significant increase in Al_{PP} phase was shown for coarse basalt. Meso-density fraction also showed significant enrichment of Fe_{OX} for both basalt treatments and that of Al_{OX} for the coarse basalt treatment relative to Si_{OX} (Table 3). In addition, Fe_{OX} phase appeared to be enriched relative to Al_{OX} phase in fine basalt treatment. The carbon-to-extractable metal

molar ratios ranged from 0.5 to 2.3 (Table S12).

total extractable metals, from the sequential PP, OX, and DC extractions, in LF+MF in the coarse basalt and fine basalt treatments increased from 1.11.1 1.31.2 to 1.41.4 3.13.1 mg g⁻¹ bulk for Al and from 3.93.9 4.54.5 to 5.45.4 1313 mg g⁻¹ bulk for Fe during the 55-day incubation (Table S5910-2; Table S61011). In HF, on the other hand, the total extractable Al slightly decreased from 5.14.2 6.04.9 to 3.73.7 4.14.1 mg g⁻¹ bulk, and that of Fe decreased from 3428 3630 to 2525 2929 mg g⁻¹ bulk during the incubation. The LF isolated after the incubation contained low amounts of extractable Al, Fe, and Si with some variations among the treatments (Table S61011). Higher concentrations of extractable Al and Fe in LF and HF were found in the two basalt treatments compared to the granite and sand treatments. When summing up the total extractable Al, and Fe, and Si among the three fractions, the significant increase over the incubation period was detected only for Al (1.49 ± 0.251.7 mg g⁻¹ bulk) and Fe (5.10 ± 1.786.8 mg g⁻¹ bulk) from the fine basalt treatment. Thus, the observed changes in the extractable metals among the fractions resulted from both chemical weathering and redistribution for the fine basalt and only from redistribution for the other treatments.

Table 2. Concentrations (per fraction) of extractable Al, Fe, and Si in each density fraction from the mineral-OM mixture/rock-OM mixtures on Day 55.

	Sodium-pyrophosphate (PP)			Acid-oxalate (OX)			Dithionite-citrate (DC)		
	Al	Fe	Si	Al	Fe	Si	Al	Fe	Si
<i>Low-density fraction (<1.8 g cm⁻³)</i>									
Granite 38- 75 µm	0 ± 3	0 ± 5	0 ± 0	1 ± 0	1 ± 7	0 ± 1	0 ± 0	1 ± 5	2 ± 7
Basalt 38- 75 µm	0 ± 8	0 ± 3	0 ± 2	1 ± 4	3 ± 3	0 ± 7	0 ± 7	2 ± 1	4 ± 0
Basalt 20- 38 µm	0 ± 2	0 ± 1	0 ± 2	2 ± 1	6 ± 3	1 ± 2	0 ± 8	3 ± 3	6 ± 4
Sand 100- 300 µm	0 ± 9	0 ± 4	0 ± 0	1 ± 1	1 ± 6	0 ± 9	0 ± 6	1 ± 1	2 ± 4
<i>Meso-density fraction (1.8-2.4 g cm⁻³)</i>									
Granite 38- 75 µm	N.A.	N.A.	N.A.	N.A.	N.A.	N.A.	N.A.	N.A.	N.A.
Basalt 38- 75 µm	0 ± 4	0 ± 6	0 ± 4	1 ± 3	5 ± 3	6 ± 3	2 ± 7	1 ± 6	9 ± 6
Basalt 20- 38 µm	0 ± 4	0 ± 9	0 ± 2	1 ± 8	7 ± 4	9 ± 4	2 ± 4	1 ± 4	9 ± 2
Sand 100- 300 µm	N.A.	N.A.	N.A.	N.A.	N.A.	N.A.	N.A.	N.A.	N.A.
<i>High-density fraction (>2.4 g cm⁻³)</i>									
Granite 38- 75 µm	0 ± 0	0 ± 0	0 ± 0	1 ± 2	6 ± 8	1 ± 4	1 ± 8	1 ± 0	7 ± 3

		±		±		±													
Basalt	0	±	0	±	0	±	0	±	0	±	0	±	0	±	0	±	0	±	0
38-75	0	±	0	±	0	±	0	±	0	±	0	±	0	±	0	±	0	±	0
µm	7	±	3	±	6	±	2	±	3	±	5	±	2	±	4	±	3	±	8
Basalt	0	±	0	±	0	±	0	±	0	±	0	±	0	±	0	±	0	±	0
20-38	0	±	0	±	0	±	0	±	0	±	0	±	0	±	0	±	0	±	0
µm	5	±	8	±	7	±	2	±	2	±	4	±	9	±	5	±	9	±	6
Sand	0	±	0	±	0	±	0	±	0	±	0	±	0	±	0	±	0	±	0
100-	0	±	0	±	0	±	0	±	0	±	0	±	0	±	0	±	0	±	0
300	0	±	0	±	0	±	0	±	0	±	0	±	0	±	0	±	0	±	0
µm	0	±	0	±	0	±	0	±	5	±	8	±	4	±	7	±	4	±	2

Al, Fe, and Si were extracted sequentially with sodium pyrophosphate, acid oxalate, and dithionite-citrate.

Value shows mean ± standard deviation ($n = 3$).

N.A. Not analyzed due to limited mass recovery of MF meso-density fraction.

Concentrations (per fraction) on Day 0 are represented in Table S910-1.

When focusing on MF, statistically detectable increase (thus accumulation) of extractable metals and metalloid during the incubation was found only for the fine basalt treatment (Fig. 5). On the other hand, the coarse basalt treatment showed a small but significant increase in Al_{pp} in MF during the incubation ($P < 0.01$, Fig. 5a). For the two basalt treatments, the amounts of Al_{OX} and Fe_{OX} in MF on Day 55 accounted for 82–87% and 76–83% of the total extractable metal pools (i.e., the sum of PP, OX, and DC extractions), respectively (Table S61011). The fine basalt treatment significantly increased the amounts of Al, Fe, and Si in MF for all three extractable phases during the incubation ($P < 0.05$) (Fig. 5). On the other hand, the coarse basalt treatment showed a small but significant increase in Al_{pp} in MF during the incubation ($P < 0.01$, Fig. 5a). The fine basalt treatment had significantly higher amounts of extractable Al, Fe, and Si in MF than the coarse basalt treatment for all extractable phases on Day 55 ($P < 0.05$, Fig. 5; Table S6). In addition, the amount of extractable Ca in MF also showed a significant increase for PP and DC extractable phases in both basalt treatments during the incubation ($P < 0.01$, Fig. S3). Note that we did not detect OX extractable Ca, presumably due to the precipitation of calcium oxalate. The interpretation of extractable Ca in the current study needs some caution. When summing up the total extractable Al and Fe among the three fractions, a significant increase after the incubation period was detected for Fe (7.2 mg g^{-1} bulk) and Al (1.7 mg g^{-1} bulk) only in fine basalt treatment (Table S10-2, S11). Thus, the observed changes in the extractable metals among the fractions likely resulted from both basalt weathering and redistribution in fine basalt and only from the redistribution in the other treatments.

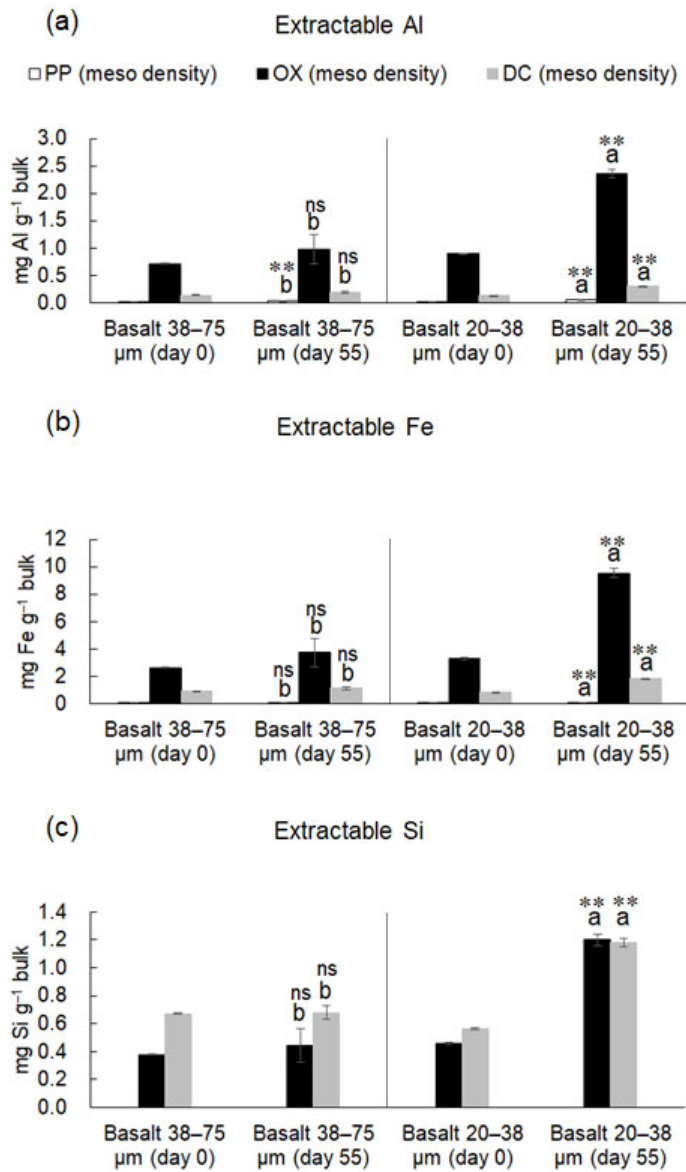


Figure 5. Amounts of extractable Al (a), Fe (b), and Si (c) in MF from the mineral-OM mixture/rock-OM mixtures on Day 0 and Day 55. See Figure 3 figure legend for s. The extractions were done sequentially with sodium pyrophosphate (PP), acid oxalate (OX), and dithionite-citrate (DC). Statistical significant difference signs. s among the rock treatments on Day 55 are shown by different letters at $P < 0.05$ (Tukey's test; $n = 3$). The increase in extractable metal from Day 0 to Day 55 is shown with asterisks (** significances at $P < 0.01$; ns, not significant). The same letters in each extraction (i.e., PP, OX, or DC) on Day 55 are not significantly different at $P < 0.05$ (Tukey's test; $n = 3$). Differences between the "on Day 0" and "on Day 55" in each mineral-OM mixture and each extraction (i.e., PP, OX, or DC) are significant at * $P < 0.05$, ** $P < 0.01$; ns, not significant (t test).

We further assessed the stoichiometry of the major elements accumulated in MF during the incubation. The carbon-to-extractable metal ratios in moles ranged from 0.5 to 2.3, and C was more enriched for Fe than Al in both basalt treatments (Table S71112). Over the 55-day incubation, we detected significant enrichment of Fe_{OX} for both basalt treatments and that of Al_{OX} for the coarse basalt treatment relative to Si_{OX} (Table 3). Moreover, the $Fe_{OX}:Al_{OX}$ ratio showed a significant increase in the fine basalt treatment.

The $pH_{(H_2O)}$ of the bulk samples of all treatments on Day 55 ranged between 6.5 and 7.6, with the highest pH in the fine basalt treatment, followed by the coarse basalt, while the granite and sand treatments were slightly acidic (Table 4). The difference in $pH(KCl)$ among the treatments was less clear.

Table 3. Molar ratios of acid oxalate extractable Al, Fe, and Si in meso-density fraction MF in the two basalt treatments before and after the 55-day incubation.

		Meso-density fraction (1.8–2.4 g cm ⁻³)					
		Al:Si		Fe:Si		Fe:Al	
Basalt 38–75 μm	Day 0	2.0	± ≤0.10	3.5	± ≤0.10	1.8	± ≤0.10
	Day 55	2.3	± ≤0.10 **	4.2	± 0.1 **	1.8	± ≤0.10 ns
Basalt 20–38 μm	Day 0	2.0	± ≤0.10	3.6	± ≤0.10	1.8	± ≤0.10
	Day 55	2.0	± ≤0.10 ns	4.0	± ≤0.10 **	2.0	± ≤0.10 **

Value shows mean ± standard deviation ($n = 3$).

Differences between the “on Day 0” and “on Day 55” in each treatment are significant at $**P < 0.01$; ns, not significant (t -test). The increase in molar ratio from Day 0 to Day 55 is shown with asterisks (** significance at $P < 0.01$; ns, not significant, t -test).

Table 4. pH of the mineral-OM mixture and rock-OM mixtures after the 55-day incubation.

	pH(H ₂ O)			pH(KCl)		
Granite 38–75 μm	6.7	± ≤0.10	c	6.1	± ≤0.10	a
Basalt 38–75 μm	7.3	± ≤0.10	b	5.9	± ≤0.10	bc
Basalt 20–38 μm	7.6	± ≤0.10	a	6.0	± ≤0.10	ab
Sand 100–300 μm	6.5	± ≤0.10	d	5.8	± ≤0.10	c

Value shows mean ± standard deviation ($n = 3$).

Means followed by the same letter are not significantly different at $P < 0.05$ (Tukey’s test; $n = 3$). Significant differences among the rock treatments on Day 55 are shown by different letters at $P < 0.05$ (Tukey’s test; $n = 3$).

3.4 Leaching loss of elements and leachate chemistry

The total amount of DOC released from the mineral-OM mixture and rock-OM mixtures during the eight repeated leaching events was 13–15 mg C per incubation column (Table 5), which was equivalent to 1.3–1.5% of the total C in the initial mixtures. No significant difference in DOC release was found among the four treatments. For the major rock-forming elements, Fe leaching was the highest in the fine basalt, followed by the coarse basalt treatment, and Si leaching showed similar patterns (Table 5). Conversely, the total amount of Al leached was the highest in the sand and the lowest in the coarse basalt treatment. The sum of base cations leached was the highest in the fine basalt treatment, followed by the coarse basalt, sand, and granite treatments. Leaching of base cations during the incubation followed the order: Ca > Na > K > Mg. Greater leaching of Na from fine basalt relative to coarse basalt was consistent with (Yang et al., 2026), which likely indicates rapid dissolution of Na plagioclase from the basaltic rock (Yang et al., under revision/accepted). The pH of the leachates was neutral to alkaline (7.1–9.1), with the highest pH in the fine basalt, followed by the coarse basalt treatment, while the other two treatments had nearly neutral pH (Table 4). The observed pH difference largely corresponded to the variation of the leachate chemistry among the treatments (e.g., Na, Ca, and Al).

Table 5. Amounts of DOC, Al, Fe, Si, base cations, and pH in leachates released from the mineral-OM mixture and rock-OM mixtures during the 55-day incubation (the sum of the eight repeated leaching events).

	DOC			Al			Fe			Si		
	(mg)			(mg)			(mg)			(mg)		
Granite 38–75 μm	14	± 1	a	0.0068	± 0.0019	ab	0.015	± 0.001	c	1.5	± 0.1	b
Basalt 38–75 μm	13	± ≤10	a	0.0044	± 0.0007	b	0.028	± 0.001	b	3.5	± ≤0.10	a

590

Basalt 20–38 μm	15	$\pm \leq 1.0$	a	0.0060	± 0.0009	ab	0.036	$\pm \leq 0.0010$	Aa	4.5	± 0.2	a
Sand 100–300 μm	13	± 1	a	0.010	± 0.001	a	0.013	$\pm \leq 0.0010$	Cc	1.7	± 0.4	b

	Sum of base cations (mg)		Na (mg)		Ca (mg)		K (mg)		Mg (mg)		pH					
Granite 38–75 μm	7.7	± 0.3	c	1.6	$\pm \leq 0.10$		4.2	± 0.2	0.94	± 0.06		1.0	± 0.1	7.2	$\pm \leq 0.10$	c
Basalt 38–75 μm	9.8	± 0.3	b	2.0	± 0.1		5.5	± 0.2	1.7	$\pm \leq 0.10$		0.62	± 0.04	7.9	± 0.1	b
Basalt 20–38 μm	14	$\pm \leq 1.0$	a	6.1	± 0.2		5.4	± 0.1	1.6	$\pm \leq 0.10$		0.49	± 0.02	9.1	$\pm \leq 0.10$	a
Sand 100–300 μm	8.9	± 0.7	bc	1.2	± 0.2		3.3	± 0.4	3.3	± 0.3		1.1	± 0.1	7.1	± 0.1	c

Value shows mean \pm standard deviation ($n = 3$).

Significant differences among the rock treatments on Day 55 are shown by different letters at $P < 0.05$ (Tukey's test; $n = 3$). Means followed by the same letter are not significantly different at $P < 0.05$ (Tukey's test; $n = 3$).

595

3.5 Microscopic observations of organo-mineral assemblage by SEM and STXM-NEXAFS

We observed some shaking-resistant, organo-mineral assemblages in the post-incubation MF (Fig. 6). The observed assemblages were present as microaggregates of 100–200 μm in diameter, consisting of crushed rocks (Fig. 6b, 6d, 6f) and OM, including fungal hyphae (Fig. 6d). Greater aggregate sizes were apparent in the two basalt treatments compared to the granite treatment (Fig. 6d, 6f). Much finer subunits (rock fragments) were confirmed in the fine basalt aggregates compared to the coarse basalt aggregates.

600

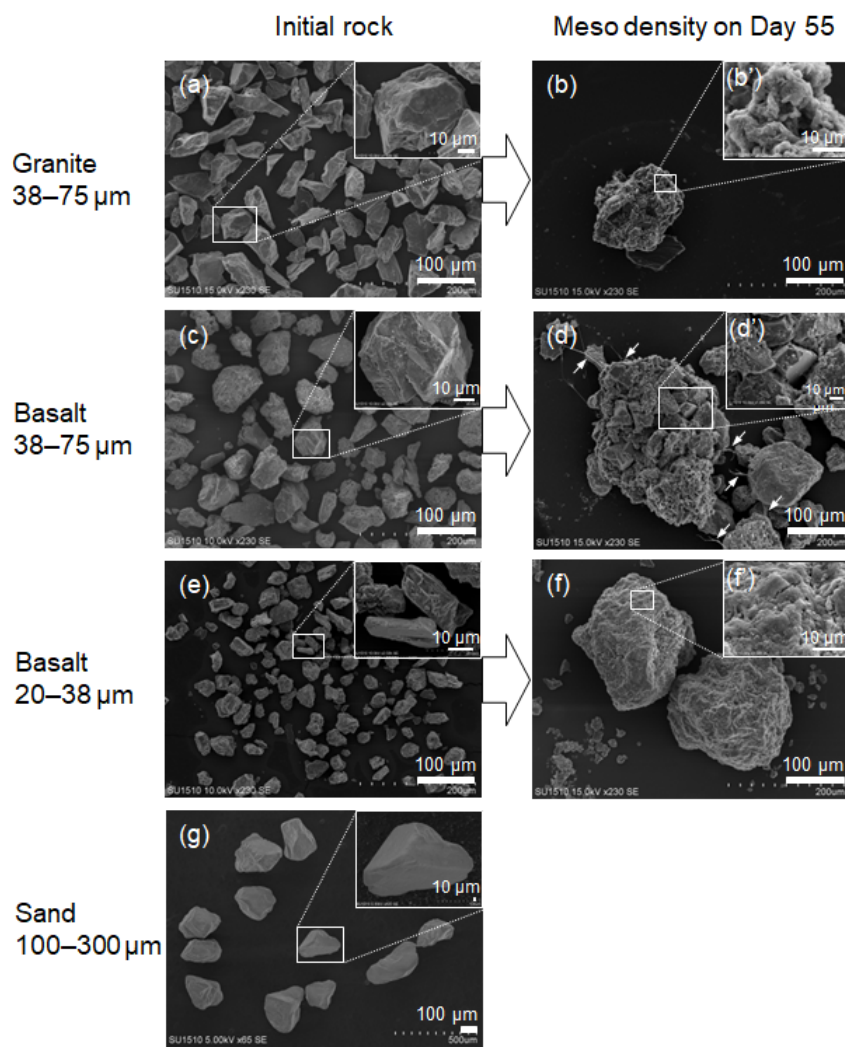


Figure 6. SEM images of the crushed rock minerals and the isolated density fraction. (a) initial granite ~~mineral~~, (b) MF of granite, (c) initial coarse basalt ~~mineral~~, (d) MF of coarse basalt, (e) initial fine basalt ~~mineral~~, and (f) MF of fine basalt, and (g) initial sand. ~~Fungal hyphae were shown with arrows (d).~~

The subsamples of dispersed MF material from the selected ~~mineral-OM mixture~~ rock-OM mixtures, the granite and coarse basalt treatments (see Fig. S4 for SEM images), were further characterized to assess the chemical nature of the organo-mineral assemblages by STXM-NEXAFS (Fig. 7). ~~Fine basalt treatment was not analyzed due to the limited beamtime.~~ We first obtained the spatial distribution of C, Al, and Fe for a large area ($35 \times 35 \mu\text{m}$, Fig. 7A, 7B). As the C-rich zones in the targeted assemblage were patchy, we selected one of these patches and the adjacent mineral-rich zones as a focused area ($5 \times 5 \mu\text{m}$) to examine the distribution of C functional groups (Fig. 7a, 7b). ~~The submicron spatial heterogeneity was present for C within the $5 \times 5 \mu\text{m}$ areas.~~ In the granite sample, the C-rich zone (shown as ROI in Fig. 7a) was relatively enriched in aromatic and, ~~to a lesser extent~~, carboxylic C compared to the average C K-edge NEXAFS spectra of the ~~entire~~ whole $5 \times 5 \mu\text{m}$ area (Fig. 7a1, 7a3). ~~The spatial distribution of the two C functional groups was similar (Fig. 7a1, 7a3).~~ While some overlaps of C with Fe and Al (Fig. 7a4, 7a5) were shown, the metal-rich patches appeared to be present adjacent to, rather than overlapped with, the C-rich zone. The dominance of Fe over Al shown in the ~~fine~~ coarse basalt treatment (Fig. 7B) was in line with the higher content and increase of FeO_x relative to AlO_x phase (Fig. 5a, 5b). In the coarse basalt sample, ~~by contrast~~, the C-rich zone (ROI in Fig. 7b) was enriched in ketonic C in contrast with the granite sample ~~compared to the average C of the whole area~~ (Fig. 7b2). Aromatic C and carboxylic C appeared to be distributed separately (Fig. 7b1, 7b3). ~~The distributions of Fe and Al were not successfully measured.~~ While the three major C peaks were found in MF ~~from~~ of both granite and coarse basalt ~~treatments~~, the latter appeared to have a higher relative abundance

of ketonic C (Fig. 7, middle left spectra).

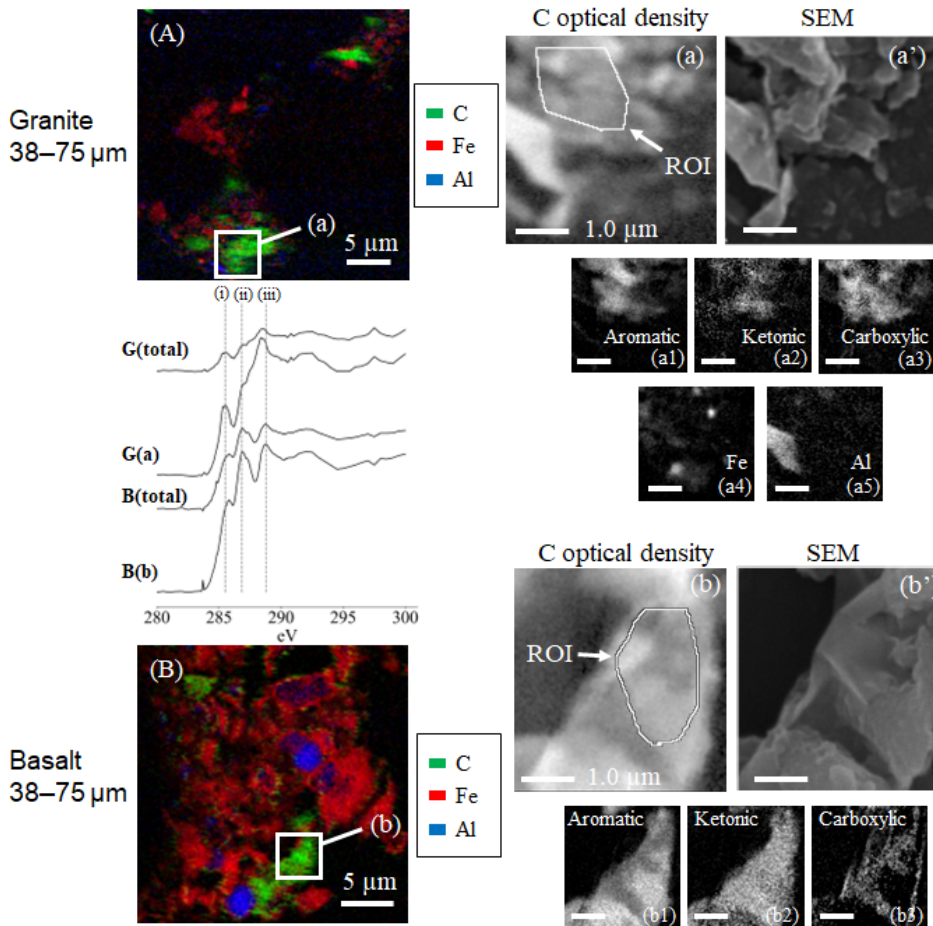


Figure 7. The elemental maps obtained with STXM-NEXAFS analysis. The images show the distribution of elements in the 35 x 35 μm region of interest for MF of granite (A) and 30 x 30 μm region of interest for coarse basalt treatments (B) after the 55-day incubation, respectively. C optical density (a, b) and SEM (a', b') images for a selected C-rich region at higher resolution (5 x 5 μm and 4 x 4 μm, respectively). The C K-edge NEXAFS spectra in the middle left panel show the image stacks for the 35 x 35 μm region of granite, G(total), and coarse basalt, B(total), and for the C-rich regions of granite, G(a), and coarse basalt, B(b). Dashed lines (i), (ii), and (iii) represent the energy levels at 285.5, 286.8, and 288.8 eV corresponding to aromatic C, ketonic C, and carboxylic C. The images (a1), (a2), and (a3) and (b1), (b2), and (b3) show the spatial distribution of specific C type, aromatic C, ketonic C, and carboxyl C, respectively, in the higher resolution images. The distribution of Fe (a4) and Al (a5) was measured only for the granite sample due to beamtime limitations. The elemental maps obtained with STXM-NEXAFS analysis. The images show the distribution of elements in the 35 x 35 μm region of interest for MF of granite (A) and coarse basalt treatments (B) after the 55-day incubation, respectively. The images (a) and (b) show the C optical density for a selected C-rich region at a higher resolution (5 x 5 μm). The C K-edge NEXAFS spectra at middle left panel show the image stacks for the total 35 x 35 μm region of granite, G(total), and that of coarse basalt, B(total), and for the C-rich region spectra of granite, G(a), and coarse basalt, B(b). The dashed lines (i), (ii), and (iii) represent the energies at 285.5, 286.8, and 288.8 eV corresponding to aromatic C, ketonic C, and carboxylic C. The images (a1), (a2), and (a3) and (b1), (b2), and (b3) show the spatial distribution of specific C type, aromatic C, ketonic C, and carboxyl C, respectively, in a 5 x 5 μm region. The image (a4) and (a5) shows the spatial distribution of Fe and Al in the same area corresponding to the image (a).

3.6 Bacterial community composition after the 55-day incubation

We assessed the effect of the mineral treatment/rock treatment on the microbial community composition at the end of the incubation using bacterial amplicon sequencing. The bacterial copy number ranged from 3.7×10^8 to 1.5×10^9 , and the initial compost tended to have a higher number than the bulk samples after the incubation (Table S8-1213). Among the post-incubation bulk samples, the bacterial number decreased in the following order: sand > granite > two basalt treatments, with no significant difference among the treatments (ANOVA, $P = 0.08$). The alpha diversity indices, including Chao1, Shannon index, and evenness, showed no significant differences among the treatments (Table S8-1213; ANOVA, $P = 0.28, 0.24, 0.10$, respectively). Yet Notably, the beta diversity (PCoA plot; Fig. 8a) was different among the treatments (PERMANOVA, F

=5.63, $P = 0.001$), while the top three phyla—Proteobacteria, Actinobacteria, and Firmicutes—were commonly observed across the samples (Fig.8b). The sum of the relative abundance of the three ASVs belonging to Neobacillus (Fig.8c), the most dominant genus, was higher in MF compared to the bulk sample ($15.5 \pm 8.4\%$ and $3.5 \pm 1.7\%$, respectively, t -test, $P = 0.0036$). The mantel results using the data of MF and the bulk samples on Day 55 further showed significant correlations between the microbial composition (PCoA score) and selected soil properties including total C, total N, pH(KCl), pH(H₂O), Fe_{PP}, and Al_{PP} ($R^2 = 0.86, 0.86, 0.82, 0.80, 0.30$ and 0.22 respectively, $P < 0.05$; Table S9-13-14).

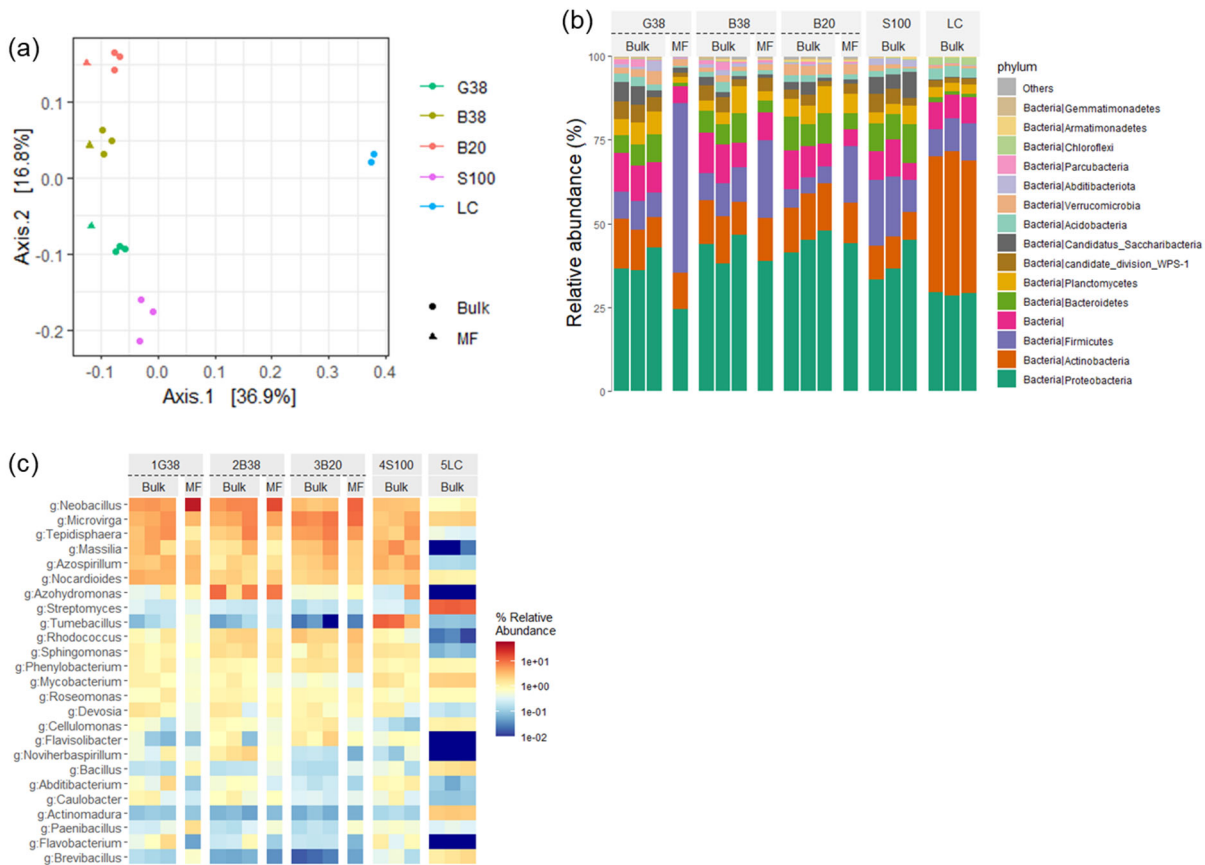


Figure 8. Beta diversity shown by PCoA plot based on 16S rRNA gene (a), bar plot at phylum level (b), and heatmap at genus level (c) in bulk and MF samples. G38: granite 38–75 μm (dDay 55), B38: basalt 38–75 μm (dDay 55), B20: basalt 20–38 μm (dDay 55), S100: sand 100–300 μm (dDay 55), and LC: initial leaf compost.

4 Discussion

4.1 Testing Formation of organo-mineral assemblages via weathering-derived metal supply of the organo-metallic glue hypothesis

We conducted a simple incubation experiment to mimic key aspects of field soil conditions, namely wet-dry cycles with water percolation and microbial heterotrophic activity to, and test whether Fe and Al released from rock weathering promote the formation of organo-mineral assemblage, represented by the meso-density fraction (MF), and to assess, along with the concurrent associated changes in both organic matter (OM) and rock-derived forming elements. Among the three crushed rocks used, the fine basalt-OM mixture, showed the highest increases in MF mass (Fig. 3a), and C content (Fig. 3b), and extractable metals and metalloid particularly (esp. Fe_{OX}, Al_{OX}, and Si_{OX}) in MF. Over the 55-day incubation period, when normalizing to the rock added, the accretion of C accumulation in an organo-mineral assemblage (i.e., in MF) during the 55-day incubation experiment was measured at 1.3 ± 0.14 mg C g⁻¹ bulk for (fine basalt), 0.9 ± 0.11 mg C g⁻¹ bulk

675 for coarse basalt), and 0.6 ± 0.10 – 0.62 ± 0.06 – 0.55 mg C g⁻¹ bulk for granite (Table S8-2, S9-2) mg C g⁻¹ rock bulk.
Extractable Fe, Al, and Si in MF also showed the same trend for the basalt treatments (Table S10-2, S11). The concurrent
enrichment While the formation of mineral-associated OM (MAOM) and co-occurred with the accretion of extractable
metals supports the idea that metal release from basalt weathering directly facilitates the formation of organo-mineral
assemblages, consistent with the ~~the~~ *organo-metallic glue* hypothesis (Wagai et al., 2020).

680 ——— The hypothesis proposes that the assemblage (aggregation) occurs through organo-metallic binding agents that can
form through organo-metal complexation and coprecipitation as well as dissolved OM sorption on secondary metal oxide
phases. Identifying the sources for the metal enrichment in MF provides insight into the formation mechanism. Mass balance
of the extractable metals before and after the incubation is, however, quite challenging due to relatively high errors in metal
extractions, especially when having multiple extractions and fractions. While our results are subject to these errors, we
685 postulated potential dynamics of Fe and Al phases for the fine basalt treatment where the largest changes were detected. On
bulk sample basis, net increases in total extractable Fe was found in MF (7.3 ± 0.7 mg Fe g⁻¹) and LF (0.9 ± 0.04 mg Fe g⁻¹)
while net decrease in HF (-0.9 ± 1.1 mg Fe g⁻¹) during the incubation period (Fig. 9). Then, the net increase of 7.2 ± 1.8
mg Fe g⁻¹ (i.e., LF + MF + HF) likely resulted from the basaltic rock weathering. Unfortunately, we did not detect the net Fe
increase when comparing the bulk samples before and after the incubation (data not shown) presumably due presumably to
690 errors associated with colloidal Fe (e.g., for colloidal Fe even after high-speed centrifugation, Wagai et al., 2018). On the
other hand, mass balance was more reasonable for the total extractable Al: the increase in MF (1.7 ± 0.1 mg Al g⁻¹) and LF
(0.1 ± 0.01 mg Al g⁻¹) and concurrent decrease in HF (0.1 ± 0.1 mg Al g⁻¹) resulted in the net increase in 1.7 ± 0.2 mg Al
g⁻¹ (Fig. 9), which was relatively close to the net increase detected in bulk sample ($+0.4 \pm 0.2$ mg Al g⁻¹). These results,
thus, suggest that nearly all Fe and Al released from basaltic rock may be preferentially retained in MF, even though
695 approximately 80% of the basalt particles themselves were present in HF (Table S-66). In other words, the majority of
weathering-derived Fe and Al appeared to be present transformed into as precipitates of organo-metallic phase complexes or
coprecipitates rather than secondary mineral phases (e.g., ferrihydrite). If the metals had precipitated primarily as secondary
minerals, they should have been more concentrated in HF as coatings on basalt particle surfaces. Instead, their enrichment in
MF (and, to some extent, in LF) found here implied preferential metal association with OM supports the dominance of metal-
700 organic phases.

——— We, therefore, infer that the metals (and metalloids) released from basaltic rock rapidly complexed with, or
coprecipitated with, dissolved OM and fine-sized, originating from decomposing particulate OM (POM) derived from leaf
compost, prior to the formation of, before secondary metal oxide mineral formation could occur. The metal- and OM-rich
phases resulting organo-metallic material likely enhanced particle cohesion by linking acted as effective “glues” that linked
705 less reactive constituents particles (basalt grains and residual POM), thereby promoting the formation of ing-physically
stable organo-mineral assemblages represented by MF. The inferred is mechanistic sequence – metal release → preferential
association with OM organic complexation → aggregation – provides direct experimental support for the *organo-metallic
glue* hypothesis, as depicted in (Fig. 10).

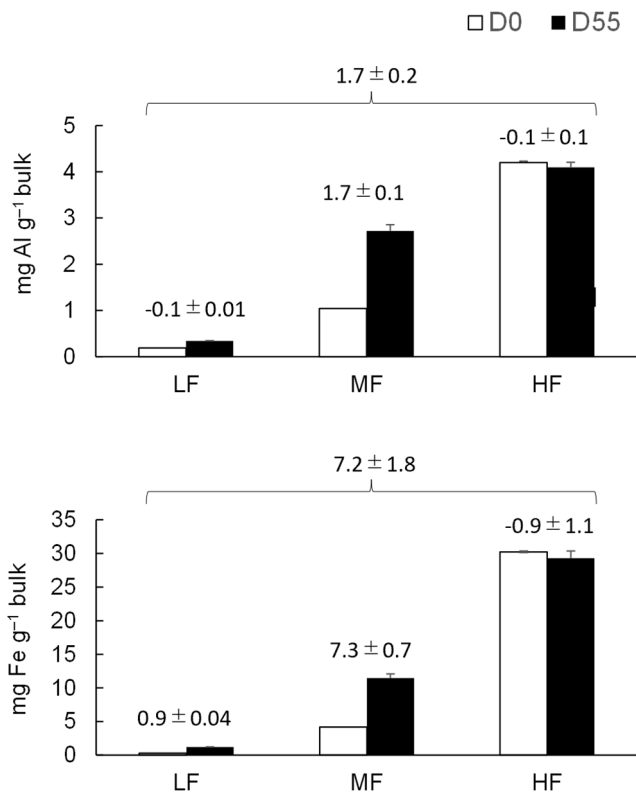


Figure-9. The changes in total extractable Al (a) and Fe (b) before and after the 55-day incubation in LF, MF, and HF on a bulk sample mass basis. Values \pm SD above the two columns represent the change from Day 0 to Day 55. The sum of the changes across LF, MF, and HF was shown on the top of the three fractions.

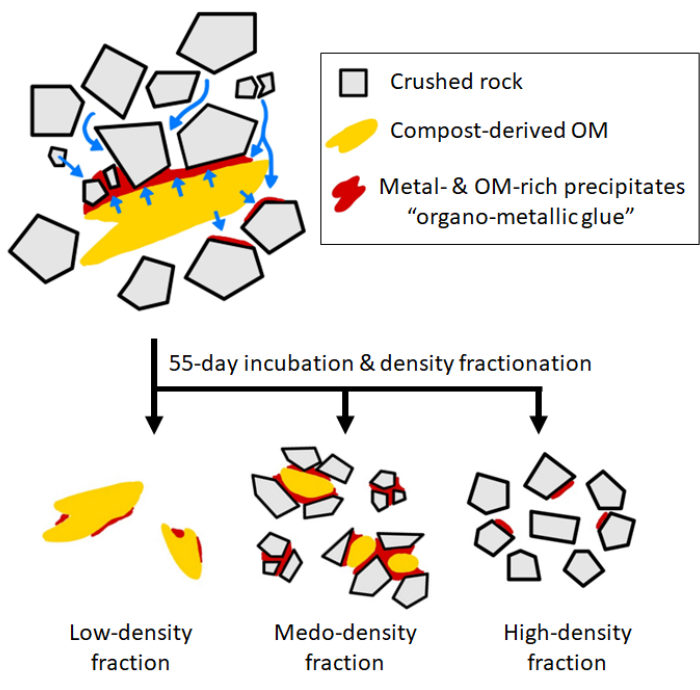


Figure 10. Conceptual synthesis of the experimental results in the context of the organo-metallic glue hypothesis. Metals (primarily Fe and Al) released from crushed rock under wet conditions were preferentially associated with dissolved and particulate OM, forming organo-metallic precipitates on mineral and organic particle surfaces upon drying. Following eight wet-dry cycles with physical mixing, these precipitates became enriched in the meso-density fraction, supporting their role as “glue” to bind mineral and organic particles to form physically stable organo-mineral aggregates.

4.2. Chemistry of the organo-mineral assemblages

Chemical characterization of MF provides further insights into the nature of the presumed organo-metallic glue. The

725 dominance of Fe_{OX} and Al_{OX} relative to Fe_{PP} and Al_{PP} phases in the basalt treatments (Table S4011) indicates that readily soluble organo-metal complexes were minor. The ~~accreted~~accreted OM in MF was thus more likely to be associated with Fe_{OX} and Al_{OX} phases through adsorptive or coprecipitation mechanisms. Microscopic observation of a representative MF microaggregate in the coarse basalt treatment (Fig. 7B) showed Fe dominance with patchy distributions of Al and C (rich in ketonic C). This pattern implies that Fe_{OX} phases (as inferred from Fig. 5b) might have entrapped small OM-rich domains during coprecipitation. Given that only a limited area was analyzed, broader generalization across all MF materials is not warranted.

730 ~~_____~~The C: (Fe+Al) molar ratio of newly-formed MF is consistent with~~supports~~ the coprecipitate interpretation. For the fine basalt treatment, the ratio of 0.58 ± 0.03 (mol:mol), after accounting for the total extractable metals originally present in the basalt, ~~fall~~falls within the range reported for laboratory-synthesized Fe-OM, Al-OM, and Fe-Al-Si-OM coprecipitates (Kleber et al., 2015; Tamrat et al., 2019; Jamoteau et al., 2023). This ratio was substantially lower than those for MF in natural soils (Wagai et al., 2020) and for organo-metal complexes typical of Andisols and spodic horizons (Takahashi and Dahlgren, 2016; Lundström et al., 2000), suggesting that the MF formed in our experiment contained relatively metal-rich, OM-poor ~~eo~~precipitates. ~~_____~~The relatively low C:metal ratios coincide with enrichment of Fe_{OX} and, to some extent, and Al_{OX} relative to Si_{OX} (Table 3), implying a greater role of Fe_{OX}~~ox~~ phase for the organo-mineral assemblage formation. Assuming that the weathering-derived Fe_{OX} phase (Fig. 5b) consists entirely of ferrihydrite, the accreted OM in MF corresponds to 108 ± 6 mg C g⁻¹ oxide – a value comparable to the maximum sorptive capacity of ferrihydrite for dissolved OM under laboratory conditions (Tipping, 1981; Kaiser et al., 1997). ~~Second, in both basalt treatments, MF was significantly enriched in Fe_{OX} and Al_{OX} relative to Si_{OX} after the incubation, except for the fine basalt treatment, where Al_{OX}:Si_{OX} ratio remained constant (Table 3). The observed Al_{OX}:Si_{OX} molar ratios of 2.0-2.3 are consistent with SRO aluminosilicate, such as allophane and imogolite (Watanabe et al., 2023). Their formation during the current incubation is difficult to judge because we were not able to detect significant increase in extractable Si on bulk scale while significant increase in Si_{OX} phase from MF was found (Fig. 5c). The increased ratios over the incubation (Table 3), nonetheless, suggest a greater role of Fe_{OX} phase such as ferrihydrite and nanocrystalline goethite relative to Si_{OX} for the assemblage formation in MF.~~

745 This result suggests that the surface of Fe_{OX} mineral phase was nearly saturated by OM, supporting the interpretation that Fe driven coprecipitation is the dominant process behind the ‘gluing’ mechanism.

750 The metal- and OM-rich phases observed in MF may reflect either coprecipitation of metals with organic ligands or the spatial co-occurrence of metal oxides and OM (e.g., OM sorption on oxides or metal precipitation on organic surfaces). Because these two mechanisms cannot be distinguished with the available data, we collectively refer to the resulting phases as organo-metallic precipitates (Fig. 10).

755 ~~_____~~We made a first-order approximation of the organo-metallic precipitates~~material~~, recognizing that the calculation relies on simplified assumptions that Fe and Al occurred as ferrihydrite and allophane and OM consisted of 50% C. This component accounted for approximately a quarter of the total MF mass, suggesting that resultant Fe-Al-OM ~~eo~~precipitates may be abundant enough to bind the ~~remining~~remaining solids (mainly basalt particles with minor POM) into stable organo-mineral assemblages (Fig. 10). In addition, ~~o~~Other major elements released from rocks (particularly~~esp.~~ Si and Ca) may synergistically~~synergistically~~ contribute to the assemblage formation~~aggregation~~ (Oades, 1988; Jamoteou et al., 2025). ~~_____~~These results indicate that organo-metallic glue formed in the current study is best described as Fe- and Al rich ~~eo~~precipitates, rather than OM dominated complexes. While the underlying mechanisms behind these associations require careful evaluation (Wagai and Mayer, 2007; Hall and Thompson, 2022; Fukumasu et al., 2025), the current results suggested a rapid formation of organo-mineral assemblage as meso-density aggregates, ~~these rock-forming elements could come from two sources—~~inherent extractable metals (e.g., secondary minerals present in the crushed basalt) and weathering-derived metals during the incubation. In the fine basalt where significant increases in extractable Al and Fe were found on a bulk

765 basis (section 3.3), we estimated that up to 62.100% of Al and 50.107% of Fe accreted in MF derived from the basalt weathering during the experiment, while the rest resulted from the redistribution/transfer from HF (i.e., preferential metal enrichment in MF). While co-localization of OM and pedogenic metal phases in various MAOM fractions has been shown across a range of soils (Wagai et al., 2020 and the reference therein), the formation rate of organo-mineral assemblage or the metal source remained unclear. The fine basalt treatment in the current experiment demonstrated the rapid assemblage formation and its direct linkage to weathering-derived metal supply, supporting the organo-metallic glue hypothesis.

770 Multiple lines of evidence point to the preferential accretion of microbially processed, N-rich OM during the organo-mineral assemblage formation. First, the C:N ratio of OM in MF sample was significantly lower than that in LF in all four mineral-OM mixture/rock-OM mixtures on Day 55 (Fig. 4a). Second, MF sample had higher $\delta^{13}\text{C}$ and $\delta^{15}\text{N}$ by 0.88–1.2‰ and 0.63–0.64‰ relative to LF, respectively, for both basalt treatments (Fig. 4b). The negative $\delta^{15}\text{N}$ values observed are within the common range for temperate forest leaves ($-2.8 \pm 2.0\%$; Martinelli et al., 1999) and for organic layers of forest soils in temperate climate zone ($-0.3 \pm 0.3\%$; Choi et al., 2020), which likely reflects the fact that the OM used in our study derived from tree leaves. Leaf compost itself contains a variety of plant- and microbially-derived compounds. Thus, the observed variation in OM chemistry among the fractions cannot be fully attributed to the reactions that took place during the 55-day incubation period. Our results are, nonetheless, consistent with the previous density fractionation studies that showed $\delta^{15}\text{N}$ increases with increasing soil particle density (Sollins et al., 2009; Hatton et al., 2012; Moni et al., 2012). Interestingly, while at very low C concentration, OM in HF had similar or greater microbial signatures compared to OM in MF (Table S48_1; Fig. 4b). These results imply that MF likely entrapped less microbially processed OM (e.g., decaying POM fragments) due presumably to the gluing effect of organo-metal coprecipitates whereas OM in HF is stabilized largely via adsorption on the crushed rock surfaces, as illustrated in the conceptual model previously (Wagai et al., 2020). Our results are also in line with the direct evidence that N-rich OM was preferentially bound to the mineral surface at the single-digit nanometer scale in an Andisol (Possinger et al., 2020). Third, the STXM-NEXAFS analysis (Fig. 7) further demonstrated that the C spectra of MF were comparable to those of soil OM (Solomon et al., 2012; Chen et al., 2014; Prietzel et al., 2018), which is dominated by microbially-processed OM in mineral soils (Sollins et al., 2009; Heckman et al., 2022). Our incubation condition (repeated wet and dry cycles and inoculation at each cycle) might have promoted the supply and turnover of microbial cell debris (Krause et al., 2019).

790 The formation of organo-mineral assemblage from the basalt-derived mixtures, along with the preferential accumulation of N-rich OM in MF, indicates a connection between microbial heterotrophic activity, chemical weathering, and aggregation. Microbes directly and indirectly promote rock and mineral weathering via mineral disaggregation, hydration, and dissolution (Banfield et al., 1999; Burghel et al., 2015; Finlay et al., 2020). Metals released by weathering may precipitate on the surface of cells or biofilms as low-crystallinity Al and Fe oxides and silicates (Lybrand et al., 2019) that are mostly extractable by the acid-oxalate method. In our study, more C was retained in MF under the treatments with higher reactive metal concentrations (Fig. 3b; Fig. 5), suggesting that the heterotrophic activity might have slowed down due to the higher abundance of reactive metals, slightly higher pH (Table 4), and greater aggregate formation (Fig. 3a). The microbial community was significantly different among the treatments on Day 55 especially between the two basalts and the other two treatments (Fig. 8) e812 while the bacterial copy number and species richness remained similar (Table S812). We noted that the most abundant genus found in the studied samples, *Neobacillus*, was more enriched in MF compared to the bulk fraction, regardless of the treatments (Fig. 8c). To the extent that this genus tends to have biomineralization attributes (Farda et al., 2022; Bhattacharjee et al., 2023), our 16S amplicon results support the idea that MF is a hotspot of intimate microbe-mineral interaction (e.g., mineralosphere, Uroz et al., 2015).

4.2 Chemistry of the organo-mineral assemblage formed

We further assessed the nature of organo-mineral assemblage based on the chemical composition of MF formed during the 55-day incubation experiment. For the two basalt treatments, the C to metal (Fe+Al) ratio in MF was calculated by accounting for the extractable metals present in the initial rocks. When summing up the three extractions for metal, the C:metal ratio was 0.36 ± 0.01 and 0.64 ± 0.21 (mol:mol) for the fine and coarse basalt, respectively. The observed ratios were within the range found in the coprecipitates formed between low molecular weight OM and rock-derived metals and metalloids in solution (Tamrat et al., 2019; Jamoteau et al., 2023) and lower than the typical ratios reported for the organo-metal complexes in Andisols and spodic horizon (Takahashi and Dahlgren, 2016; Lundström et al., 2000). In our experiment, the formation of the pedogenic metal phase mainly occurred as the Fe_{Ox} phase (Fig. 5b). Assuming ferrihydrite for this phase, the accreted OM in MF was equivalent to $68.2 \pm 1.3 \text{ mg C g}^{-1}$ oxide. This value is comparable to the maximum sorptive capacity of ferrihydrite under laboratory conditions (Tipping, 1981; Kaiser et al., 1997). In theory, sorption alone could account for the observed levels of OM; however, coprecipitation, which includes sorptive associations, cannot be excluded. Based on these considerations, we propose that the organo-metal associations formed in MF under the basalt treatments are best characterized as organo-metal coprecipitates in which accreted OM exists both as adsorptive associations with Fe-rich secondary mineral phase (e.g., Wagai and Mayer, 2007) and as complexes with released metal cations and metalloids (e.g., Jamoteau et al., 2023).

Further assessment of the stoichiometric relationship gave hints on the nature of the organo-metal coprecipitates found in MF. First, roughly two orders of magnitude higher formation of Fe_{Ox} and Al_{Ox} phases compared to Fe_{pp} and Al_{pp} phases in MF under the basalt treatments (Table S610) may suggest a greater role of adsorptive association relative to organo-metal complexation. The direct micro-scale observation of a focused region of MF aggregate in the coarse basalt treatment (Fig. 7B) showed Fe dominance with the patchy distribution of Al and C (largely ketonic), implying the major metal phase formed (i.e., Fe_{Ox} phase, Fig. 5b) might have entrapped a glob of OM. However, our observed regions were very limited, and generalization is not possible. Second, in both basalt treatments, MF was significantly enriched in Fe_{Ox} and Al_{Ox} relative to Si_{Ox} after the incubation, except for the fine basalt treatment, where $\text{Al}_{\text{Ox}}:\text{Si}_{\text{Ox}}$ ratio remained constant (Table 3). The observed $\text{Al}_{\text{Ox}}:\text{Si}_{\text{Ox}}$ molar ratios of 2.0-2.3 are consistent with SRO aluminosilicate, such as allophane and imogolite (Watanabe et al., 2023). Their formation during the current incubation is difficult to judge because we were not able to detect significant increase in extractable Si on bulk scale while significant increase in Si_{Ox} phase from MF was found (Fig. 5c). The increased ratios over the incubation (Table 3), nonetheless, suggest a greater role of Fe_{Ox} phase such as ferrihydrite and nanocrystalline goethite relative to Si_{Ox} for the assemblage formation in MF. Third, when comparing the two basalt treatments, significantly greater Fe_{Ox} formation was shown in the fine basalt (Fig. 5b), indicating higher Fe dissolution (Table 3) due possibly to higher specific surface area (Table S2), more abundant OM (which likely includes organic acids), and/or slightly more alkaline pH (Table 4). The redox regime during the incubation may also be slightly different between the two basalt treatments, as the basalt particle size should affect water and oxygen dynamics via texture/porosity difference, which might have affected Fe-OM interaction (Chen et al., 2020).

4.3. Organic matter dynamics during assemblage formation

Several lines of evidence point to preferential accretion of microbially-processed, N-rich OM during organo-mineral assemblage formation. First, the C:N ratio of OM in MF sample was significantly lower than that in LF in all four rock-OM mixtures on Day 55 (Fig. 4a), suggesting a greater contribution of microbially altered material in MF. Second, MF had higher $\delta^{13}\text{C}$ and $\delta^{15}\text{N}$ values ($+0.88$ – 1.2% and $+0.63$ – 0.64% , respectively) relative to LF in basalt treatments (Fig. 4b, 4c). The negative $\delta^{15}\text{N}$ values observed are within the common range for temperate forest leaves ($-2.8 \pm 2.0\%$; Martinelli et al., 1999) and for organic layers of forest soils in the temperate climate zone ($-0.3 \pm 0.3\%$; Choi et al., 2020), which likely

reflects tree-leaf origin of the OM used in our study. Leaf compost itself contains a variety of plant- and microbially-derived compounds. Thus, the observed isotopic enrichment in MF cannot be fully attributed fully to microbial reactions that took place during the incubation. Our results are, nonetheless, consistent with previous field studies showing the increase in $\delta^{13}\text{C}$ and $\delta^{15}\text{N}$ with soil particle density (Sollins et al., 2009; Hatton et al., 2012; Moni et al., 2012). Importantly, HF contained small amounts of even stronger stoichiometric (Table S9-1, Fig. 4a) and isotopic (Fig. 4b) microbial isotopic signatures than MF (Table S89-1; Fig. 4b, 4e). These results suggest that some of decomposing POM fragments were likely occluded in MF, while HF primarily retained adsorbed microbial OM. The role of POM in MF formation aligns with its well-known role as hotspots for microbial activity and dissolved OM production, which may induce localized dissolution of minerals (e.g., Bölscher et al. 2025).

— These findings are in line with support the conceptual framework previously proposed (Fig. 7b in Wagai et al., 2020): coprecipitation driven aggregation and OM stabilization in MF and surface adsorption dominance in HF. STXM-NEXAFS spectra (Fig. 7) further suggests that C spectra of MF resemble those of typical soil OM (Solomon et al., 2012; Chen et al., 2014; Priezel et al., 2018), which is dominated by microbially-processed OM in mineral soils (Sollins et al., 2009; Heckman et al., 2022). Our incubation conditions (wet-dry cycles, high temperature, and inoculation at each cycle) likely promoted microbial turnover and supply of microbial residues such as cell wall fragments and extracellular polymers (Kraruse et al., 2019).

— These results, collectively, indicate that organo-mineral assemblages formed in MF were enriched in microbially-processed, N-rich OM, linking microbial activity, chemical weathering, and aggregation. Microbes likely accelerated mineral weathering via disaggregation, hydration, and localized dissolution (Banfield et al., 1999; Burghlea et al., 2015; Finlay et al., 2020), releasing Fe and Al that subsequently coprecipitate with, or were sorptively associated with, microbially derived compounds on the surface of cells or biofilms as low-crystallinity Al, Fe, Si mineral phases (Lybrand et al., 2019). This process may have created reactive Fe–Al–OM phases that acted as nucleation sites for aggregation. The observed bacterial community patterns may be linked to these processes. While the community composition differed markedly among the rock treatments, 13 bacterial copy numbers tended to be lower in the basaltic treatments (Table S13) potentially reflecting the protective role of the extractable metal phases. The genus *Neobacillus*, known for its biomineralization potential (Farda et al., 2022; Bhattacharjee et al., 2023), appeared to be enriched in MF relative to the bulk fraction (Fig. 8c), supporting the idea of MF as a mineralosphere (Uroz et al., 2015) where organo-metallic coprecipitates and microbial residues interact to drive aggregation.

4.4.3 Influence of the size and chemical composition of crushed rock

Both the particle size and chemistry of the rock material crushed rock affected may control the formation of organo-mineral assemblage aggregates in MF. The mineral particle size likely played a significant role because the formation of MF, including the accretion of OM and pedogenic metal phases, occurred more in the fine basalt treatment produced significantly more MF than the coarse basalt or other treatments (Fig. 3a, 3b; Fig. 5), emphasizing the importance of mineral particle size in regulating reactivity and aggregation. However, the size effect is not straightforward. Using the basaltic rock from the same source, Yang et al. (under review accepted 2026) observed less formation of FeO_x and AlO_x phases from finer basalt due to greater occlusion of basalt particles within meso-density aggregates, which limited water access and slowed weathering. Thus, multiple factors such as the degree of drying and mixing, OM decomposability, incubation duration, and basalt particle size likely interact to produce size-dependent effects. Even small differences in pore structure or redox dynamics can strongly influence weathering and aggregation, for instance, via affecting Fe-OM interactions (e.g., Chen et al., 2020).

— In addition, the rock chemistry/real composition also influenced likely contributed to OM the observed the retention

of OM as organo-mineral assemblages in MF. Despite the similar the same size distribution class (38–75 μm) and similar particle size distribution (Fig. S2+2), the coarse basalt treatment led to had greater significantly higher OM accretion in MF with a slightly lower C:N ratio compared to the than granite treatment (Fig. 3b; Fig. 4a), which is attributable to. In addition, the initial coarse basalt had more than one order of magnitude higher initial metal contents, especially in of PP and especially OX extractable metals (Fe_{OX} , Al_{OX} , and Si_{OX}) than the initial granite (Table S2). Thus, the greater OM retention in the coarse basalt (Fig. 3b) may be attributable to the initial abundance of the reactive secondary minerals present. When The increase in OM retention in the coarse basalt relative to the granite treatment (Fig. 3b), normalized to their difference in specific surface area (Table S2), OM accretion in coarse basalt relative to granite correspond translates to additional C loading of $\approx 0.1 \text{ mg C m}^{-2}$, which lies is well within the maximum sorptive limit of capacity of the reactive secondary minerals (Wagai and Mayer, 2007; Schneider et al., 2010) and is comparable to the C loadings accretion on goethite under in temperate field conditions (Bramble et al., 2024). The strong influences significant contribution of pre-existing secondary mineral extractable metals (i.e., secondary minerals) in basaltic rock on organo-mineral associations present in the crushed basalt is consistent with findings from a similar has also been shown in another incubation experiment conducted under slightly different conditions (Yang et al., under review accepted 2026). Although our Our current study lacked did not have a “fine-sized granite” treatment for. Thus, a full factorial comparison, design experiment is necessary to fully test the relative importance of mineral size and chemistry (weatherability) on the formation of organo-mineral assemblage. the present results indicate that both particle size and mineralogy jointly regulate organo-mineral assemblage formation and OM stabilization.

4.5.4 Implications

Our Our experiment, conducted under simplified conditions, a results from the artificial soil (the mineral OM mixture rock OM mixtures) may provide mechanistic insights relevant to early-stage pedogenesis have implications for field soil processes. Weathering of crushed fragmented rock in the presence of OM and microbial activity under fluctuating water regimes a wet and dry cycle likely occur occurs during the early stages of pedogenesis (e.g., primary succession on glacial tills). Although the wet-dry cycles applied here were more intense than typical field conditions, such processes can also occur in agricultural topsoils, where physical mixing and periodic drying can promote mineral-organic interactions. Physical mixing and the severe wet and dry cycle used in this study may resemble conditions in agricultural topsoils. Recently, the application mixing of crushed basalt and other mafic rocks to soils has drawn increasing attention as a strategy for method to remove atmospheric CO_2 removal through enhanced weathering. The chemical weathering of basic rock releases divalent base cations (mainly Ca and Mg). These cations are partially balanced by carbonic acids that ultimately derive from atmospheric CO_2 (Beerling et al., 2020). Besides CO_2 removal, several recent pot- and field-scale studies have reported showed an apparent increases in soil OM following mafic rock addition upon the mixing of basic rock powders (Buss et al., 2024; Xu et al., 2024), although others found no the lack of response was also reported (Yan et al., 2023; Sokol et al., 2024). In the current study, Although we did not detect the significant change in total total C possibly did not change due possibly to the significantly after the 55-day incubation short incubation period. Another factor is carbonate formation as the incubation was done under relatively high pH conditions. However, the consistent density-dependent changes in C:N, $\delta^{13}\text{C}$, and $\delta^{15}\text{N}$ (Fig. 4, section 4.3 above) suggest that total C mainly consists of organic C with minor presence of carbonate. Regardless, our results indicated that the incorporating crushed basalt can promote the formation of stable organo-mineral assemblages via organo-metallic glue and thus potentially increase OM persistence through organo-metallic binding. On the other hand, At the same time, development of basalt-OM aggregation may reduce the rate of basalt weathering by shielding basalt mineral surfaces from further dissolution, highlighting a possible trade-off between OM stabilization and CO_2 removal efficiency (Yang et al., under review accepted 2026). Further

mechanistic studies are ~~important~~ needed to better elucidate rock-OM-secondary mineral interactions ~~quantify and to~~ optimize C ~~this~~ balance within enhanced rock-weathering strategies. Our results ~~give mechanistic support the former findings~~ studies: the incorporation of crushed basaltic rock can promote powder with organic amendments and soils likely increases the persistence of ~~formation of stable soil OM via organo-mineral assemblages and increase OM persistence through organo-metallic binding formation~~. At the same time, our finding also suggest potential negative feedback, however, ~~The formation of basalt-OM aggregates likely slows down the rate of basalt weathering rate by shielding mineral physically protecting basalt surfaces from further dissolution, highlighting a possible trade-off between OM stabilization and CO₂ drawdown efficiency in enhanced weathering scenarios (Yang et al., under review). Thus, further examination of the interactions among crushed rock, OM, and other soil particles is critical to predict the extent of CO₂ removal in enhanced rock weathering scenarios.~~

~~Across the rock treatments, Our study showed that~~ the degree of OM accretion in MF (fine basalt > coarse basalt > granite > sand, Fig. 3b) corresponded ~~closely~~ to the ~~abundance content~~ of reactive Fe_{ox}, Al_{ox}, and Si_{ox} phases (Table S2; Fig. 5) ~~both from both inherent rock composition (Table S2; Table S910-2) and weathering during incubation (Table S1011), suggesting that~~, which is likely attributed to the protective role of the reactive metal phases ~~controlled OM retention more strongly (esp. Fe_{ox}) and organo-metal coprecipitates formed more than the effect of pH (Table 4) or the bacterial abundance copy number (Table S81213). These Our results are consistent with the observations This finding may offer a mechanistic explanation for field-scale observations. First, previous studies (basaltic soils vs. granitic soils) have shown that the chemistry of parent rock strongly influences soil C storage at the landform scale (Orgill et al., 2017; Angst et al., 2018; Dutta et al., 2000; Mao et al., 2020). Basalt derived soil had a significantly greater C accumulation at 0–30 cm depth (77 t ha⁻¹) compared with granite derived soil (27–52 t ha⁻¹; Orgill et al., 2017). Another study further showed that the mean C accumulation in the upper 1-m depth soil was the highest in basalt landform (76.2 t C ha⁻¹), followed by alluvial (70.6 t C ha⁻¹), laterite (54.9 t C ha⁻¹), sandstone (48.0 t C ha⁻¹), and granite-gneiss (32.7 t C ha⁻¹) (Dutta et al., 2000). Second, the positive contribution of oxalate-extractable Fe and Al phases to soil C storage has been shown at a field scale (e.g., Fukumasu et al., 2021), regional to continental scales (Hughes, 1982; Ashida et al., 2021; von Fromm et al., 2021), up to a global scale (Rasmussen et al., 2018; von Fromm et al., 2025). The current Our~~

~~study demonstrated that organo-metallic binding and aggregation can develop rapidly through weathering and microbial processes, directly linking mineral transformation to OM stabilization and highlighting~~ While the underlying mechanisms behind these associations require careful evaluation (Wagai and Mayer, 2007; Hall and Thompson, 2022; Fukumasu et al., 2025), the current results suggested a rapid formation of organo-mineral assemblage as meso-density aggregates. The mass of assemblages—estimated assuming ferrihydrite and allophane as the mineral components—accounted for roughly one third of the total mass of the meso-density fraction (MF). It thus seems possible that the metal and OM rich assemblages formed are sticky enough to bind the other two thirds of solids (organic and basalt particles) to form meso-density aggregates, in accord with the organo-metallic glue hypothesis (Wagai et al., 2020). While the relevance of current findings to field soil processes needs to be examined further, the current results help to elucidate the intimate interactions ~~of among~~ microbes, their metabolites, and minerals in soil (Chorover, 2022; Fang et al., 2023; Wagai et al., 2023).

5 Conclusion

The formation of organo-mineral assemblages (as the meso-density fraction) from the mixture of crushed rocks and leaf compost was observed ~~within over the 55-day incubation subjected to with eight~~ wet-and-dry cycles. The extent of assemblage formation followed the sequence: fine basalt > OM mixture led to the highest formation of organo-mineral

975 assemblages, followed by the coarse basalt ~~and~~ granite ~~and~~ sand. The ~~a~~ assemblage ~~development~~ formation was driven by two coupled processes promoted by (i) microbial transformation of organic matter, evidenced re-working of OM (indicated by lower C:N and higher $\delta^{13}\text{C}$ and $\delta^{15}\text{N}$ relative to compared to the initial original leaf compost), and (ii) the supply of reactive Fe and Al, particularly extractable metals (esp. oxalate-extractable Fe, phase) from the rock weathering. The resulting chemistry of the meso-density materials formed were best characterized as organo-metallic coprecipitates enriched in both OM and oxalate-extractable Fe (and, to a less extent, Al phases, Si). These findings provide experimental support for the organo-metallic glue hypothesis (Wagai et al., 2020), demonstrating that ~~and~~ weathering-derived metals can rapidly induce aggregation and OM persistence. This mechanism links microbial activity, mineral weathering, and OM stabilization, suggesting that ~~that~~ C accretion during early-stage pedogenesis and soil OM formation are strongly controlled by the coupled action of microbial metabolism and reactive metal dynamics. ~~is likely to be driven in part by the formation of organo-mineral assemblages induced by the precipitation of short range-order metal oxides through rock weathering.~~

985 **Data availability.** ~~Available upon request. Not applicable.~~

Supplement. The supplement related to this article is available online ~~at XXXX~~.

990 **Author contributions.** KM: investigation, methodology, formal analysis, writing (original draft preparation, review, and editing); JJ: investigation; HS: investigation and formal analysis and writing (original draft preparation); EM: investigation and formal analysis and writing (original draft preparation); RS: investigation and formal analysis and writing (original draft preparation review and editing); PTY: investigation, formal analysis, and writing (review and editing original draft preparation); RW: conceptualization, methodology, formal analysis, writing (original draft preparation, review and editing), funding acquisition, and supervision.

995 **Competing interests.** The authors declare that we have no known competing financial interests or personal relationships that could have appeared to influence the work reported in this paper.

1000 **Acknowledgements.** The authors are grateful to Y. Yaegaki, R. Hirai, and Y. Yamashita for laboratory assistance; J. Fukumasu for the specific surface area analysis; K. Ito for the microbial community analysis; P. T. Yang for the XRD analysis and Y. Nakayama for technical advice during the experiment. We also thank M. Bamba, S. Sato, and K. Minamisawa (Tohoku University) for 16S rRNA amplicon sequencing.

Financial support. This paper is based on results obtained from a project, JPNP18016, commissioned by the New Energy and Industrial Technology Development Organization (NEDO).

1005 References

1010 [Amelung, W., Tang, N., Siebers, N., Aehnel, M., Eusterhues, K., Felde, Vi. J. M. N. L., Guggenberger, G., Kaiser, K., Kögel-Knabner, I., Klumpp, E., Knief, C., Kruse, J., Lehdorff, E., Mikutta, R., Peth, S., Ray, N., Prechtel, A., Ritschel, T., Schweizer, S. A., Woche, S. K., Wu, B., and Totsche, K. U.: Architecture of soil microaggregates: Advanced methodologies to explore properties and functions, *Journal of Plant Nutr. Soil Sci.*, 187, 17–50, 2024.](#)
Angst, G., Messinger, J., Greiner, M., Häusler, W., Hertel, D., Kirfel, K., Kögel-Knabner, I., Leuschner, C., Rethemeyer, J., and Muellera, C.W.: Soil organic carbon stocks in topsoil and subsoil controlled by parent material, carbon input in the rhizosphere, and microbial-derived compounds, *Soil Biol. Biochem.*, 122, 19–30,

<https://doi.org/10.1016/j.soilbio.2018.03.026>, 2018.

1015 Angst, G., Mueller, K. E., Castellano, M. J., Vogel, C., Wiesmeier, M., and Mueller, C. W.: Unlocking complex soil systems as carbon sinks: multi-pool management as the key. *Nat. Commun.*, 14, 2967, <https://doi.org/10.1038/s41467-023-38700-5>, 2023.

Arai, M., Ikazaki, K., Anzai, T., Celestial, V. P., Tumbay, J. V., Santillana, I. S., and Wagai, R.: Protective role of reactive aluminum phases to stabilize soil organic matter against long-term cultivation in the humid tropics under volcanic influence. *Soil Sci. Plant Nutr.*, 71 (1), 27–37, <https://doi.org/10.1080/00380768.2024.2415455>, 2025.

1020 Asano, M., and Wagai, R.: Evidence of aggregate hierarchy at micro- to submicron scales in an allophanic Andisol, *Geoderma*, 216, 62–74, <https://doi.org/10.1016/j.geoderma.2013.10.005>, 2014.

Ashida, K., Watanabe, T., Urayama, S., Hartono, A., Kilasara, M., Mvondo Ze, A. D., Nakao, A., Sugihara, S., and Funakawa, S.: Quantitative relationship between organic carbon and geochemical properties in tropical surface and subsurface soils, *Biogeochemistry*, 155, 77–95, <https://doi.org/10.1007/s10533-021-00813-8>, 2021.

1025 Baldock, J. A., and Skjemstad, J. O.: Role of the soil matrix and minerals in protecting natural organic materials against biological attack, *Org. Geochem*, 31 (7–8), 697–710, [https://doi.org/10.1016/S0146-6380\(00\)00049-8](https://doi.org/10.1016/S0146-6380(00)00049-8), 2000.

Bamba, M., Akyol, T. Y., Azuma, Y., Quilbe, J., Andersen, S. U., and Sato, S.: Synergistic effects of plant genotype and soil microbiome on growth in *Lotus japonicus*, *FEMS Microbiol. Ecol.*, 100 (5), fiae056, <https://doi.org/10.1093/femsec/fiae056>, 2024.

1030 Banfield, J. F., Barker, W. W., Welch, S. A., and Taunton, A.: Biological impact on mineral dissolution: Application of the lichen model to understanding mineral weathering in the rhizosphere, ~~*Proc. Natl. Acad. Sci. USA*~~, 96 (7), 3404–3411, <https://doi.org/10.1073/pnas.96.7.3404>, 1999.

Basile-Doelsch, I., Balesdent, J., and Rose, J.: Are interactions between organic compounds and nanoscale weathering minerals the key drivers of carbon storage in soils?, *Environ. Sci. Technol.*, 49 (7), 3997–3998, <https://doi.org/10.1021/acs.est.5b00650>, 2015.

1035 Beerling, D. J., Kantzas, E. P., Lomas, M. R., Wade, P., Eufrazio, R. M., Renforth, P., Sarkar, B., Andrews, M. G., James, R. H., Pearce, C. R., Mercure, J. F., Pollitt, H., Holden, P. B., Edwards, N. R., Khanna, M., Koh, L., Quegan, S., Pidgeon, N. F., Janssens, I. A., Hansen, J., and Banwart, S. A.: Potential for large-scale CO₂ removal via enhanced rock weathering with croplands, *Nature*, 583, 242–248, <https://doi.org/10.1038/s41586-020-2448-9>, 2020.

1040 Bhattacharjee, K., Barua, S., Chrungoo, N. K., and Joshi, S. R.: Characterization of biomineralizing and plant growth-promoting attributes of lithobiontic bacteria, *Curr. Microbiol.*, 80, 80, <https://doi.org/10.1007/s00284-022-03176-x>, 2023.

[Bölscher, T., Cardon, Z. G., Garcia Arredondo, M., Grand, S., Griffen, G., Hestrin, R., Imboden, J., Jamoteau, F., Lacroix, E.M., Pérez Castro, S., Persson, P., Riley, W.J., Keiluweit, M.: Vulnerability of mineral-organic associations in the rhizosphere, *Nature Comm.*, 16, <https://dx.doi.org/10.1038/s41467-025-61273-4>, 2025.](https://doi.org/10.1038/s41467-025-61273-4)

1045 Bramble, D. S. E., Ulrich, S., Schöning, I., Mikutta, R., Brandt, L., Poll, C., Kandeler, E., Mikutta, C., Konrad, A., Siemens, J., Yang, Y., Polle, A., Schall, P., Ammer, C., Kaiser, K., and Schrupf, M.: Formation of mineral-associated organic matter in temperate soils is primarily controlled by mineral type and modified by land use and management intensity, *Glob. Change Biol.*, 30, e17024, <https://doi.org/10.1111/gcb.17024>, 2024.

1050 ~~Bucka, F. B., Kölbl, A., Uteau, D., Peth, S., and Kögel-Knabner, I.: Organic matter input determines structure development and aggregate formation in artificial soils, *Geoderma*, 354, 113881, <https://doi.org/10.1016/j.geoderma.2019.113881>, 2019.~~

1055 Bucka, F. B., Felde, V. J. M. N. L., Peth, S., and Kögel-Knabner, I.: Disentangling the effects of OM quality and soil texture on microbially mediated structure formation in artificial model soils, *Geoderma*, 403, 115213, <https://doi.org/10.1016/j.geoderma.2021.115213>, 2021.

- Burghlelea, C., Zaharescu, D. G., Dontsova, K., Maier, R., Huxman, T., and Chorover, J.: Mineral nutrient mobilization by plants from rock: Influence of rock type and arbuscular mycorrhiza, *Biogeochemistry*, 124, 187–203, <https://doi.org/10.1007/s10533-015-0092-5>, 2015.
- Buss, W., Hasemer, H., Ferguson, S., and Borevitz, J.: Stabilisation of soil organic matter with rock dust partially counteracted by plants, *Glob. Chang. Biol.*, 30 (1), e17052, <https://doi.org/10.1111/gcb.17052>, 2024.
- Chapman, J. B., Weiss, D. J., Shan, Y., and Lemburger, M.: Iron isotope fractionation during leaching of granite and basalt by hydrochloric and oxalic acids, *Geochim. Cosmochim. Acta*, 73 (5), 1312–1324, <https://doi.org/10.1016/j.gca.2008.11.037>, 2009.
- Chen, C., Dynes, J. J., Wang, J., Karunakaran, C., and Sparks, D. L.: Soft X-ray spectromicroscopy study of mineral-organic matter associations in pasture soil clay fractions, *Environ. Sci. Technol.*, 48 (12), 6678–6686, <https://doi.org/10.1021/es405485a>, 2014.
- Chen, C., Hall, S. J., Coward, E., and Thompson, A.: Iron-mediated organic matter decomposition in humid soils can counteract protection, *Nat. Commun.*, 11, 2255, <https://doi.org/10.1038/s41467-020-16071-5>, 2020.
- Choi, W. J., Kwak, J. H., Park, H. J., Yang, H. I., Park, S. I., Xu, Z., Lee, S. M., Lim, S. S., and Chang S. X.: Land-use type, and land management and disturbance affect soil $\delta^{15}\text{N}$: A review, *J. Soils Sediments*, 20, 3283–3299, <https://doi.org/10.1007/s11368-020-02708-x>, 2020.
- Chorover, J.: Microbe-biomolecule-mineral interfacial reactions, in: *Multi-Scale Biogeochemical Processes in Soil Ecosystems: Critical Reactions and Resilience to Climate Changes*, edited by: Yang, Y., Keiluweit, M., Senesi, N., and Xing, B., John Wiley & Sons, Inc., Hoboken, 117–140, <https://doi.org/10.1002/9781119480419>, 2022.
- Cole, J. R., Wang, Q., Fish, J. A., Chai, B., McGarrell, D. M., Sun, Y., Brown, C. T., Porras-Alfaro, A., Kuske, C. R., and Tiedje, J. M.: Ribosomal Database Project: Data and tools for high throughput rRNA analysis, *Nucleic Acids Res.*, 42 (D1), D633–D642, <https://doi.org/10.1093/nar/gkt1244>, 2014.
- Cornell, R. M., and Schwertmann, U. (Eds.): *The Iron Oxides: Structure, Properties, Reactions, Occurrences and Uses*, Wiley - VCH Verlag GmbH & Co. KGaA, ISBN9783527602094, 2003.
- ~~Dutta, D., Sah, K. D., Reddy, R. S., Anil Kumar, K. S., and Koyal, A.: Soil organic carbon storage in different landforms of South Deccan plateau of Andhra Pradesh, *J. Indian Soc. Soil Sci.*, 48 (3), 447–450, <https://www.indianjournals.com/ijor.aspx?target=ijor:ijss&volume=48&issue=3&article=005>, 2000.~~
- ~~Ebina, T., Minja, R. J. A., Nagase, T., Onodera, Y., and Chatterjee, A.: Correlation of hydraulic conductivity of clay-sand compacted specimens with clay properties, *Appl. Clay Sci.*, 26 (1–4), 3–12, <https://doi.org/10.1016/j.clay.2003.09.010>, 2004.~~
- Edgar, R. C.: SINTAX: A simple non-Bayesian taxonomy classifier for 16S and ITS sequences, *bioRxiv*, 074161, <https://doi.org/10.1101/074161>, 2016.
- Fang, Q., Lu, A., Hong, H., Kuzyakov, Y., Algeo, T. J., Zhao, L., Olshansky, Y., Moravec, B., Barrientes, D. M., and Chorover, J.: Mineral weathering is linked to microbial priming in the critical zone, *Nat. Commun.*, 14, 345, <https://doi.org/10.1038/s41467-022-35671-x>, 2023.
- Farda, B., Djebaili, R., Del Gallo, M., Ercole, C., Bellatreccia, F., and Pellegrini, M.: The “Infernaccio” gorges: Microbial diversity of black deposits and isolation of manganese-solubilizing bacteria, *Biol.*, 11 (8), 1204, <https://doi.org/10.3390/biology11081204>, 2022.
- Finlay, R. D., Mahmood, S., Rosenstock, N., Bolou-Bi, E. B., Köhler, S. J., Fahad, Z., Rosling, A., Wallander, H., Belyazid, S., Bishop, K., and Lian, B.: Reviews and syntheses: Biological weathering and its consequences at different spatial levels – from nanoscale to global scale, *Biogeosciences*, 17 (6), 1507–1533, <https://doi.org/10.5194/bg-17-1507-2020>, 2020.
- Friedlingstein, P., O’Sullivan, M., Jones, M. W., Andrew, R. M., Gregor, L., Hauck, J., Quéré, C. Le, Luijkx, I. T., Olsen, A., and Peters, G. P., et al.: *Global Carbon Budget 2022*, *Earth Syst. Sci. Data*, 14, 4811–4900, <https://doi.org/10.5194/essd->

- 1100 Fukumasu, J., Poeplau, C., Coucheney, E., Jarvis, N., Klöffel, T., Koestel, J., Kätterer, T., Svensson, D. N., Wetterlind, J., and Larsbo, M.: Oxalate-extractable aluminum alongside carbon inputs may be a major determinant for organic carbon content in agricultural topsoils in humid continental climate, *Geoderma*, 402, 115345, <https://doi.org/10.1016/j.geoderma.2021.115345>, 2021.
- 1105 Fukumasu, J., Yang, P. T., Kajiura, M., Gregorich, E., and Wagai, R.: Soil extraction with pyrophosphate-dithionite mixture: a practical method to estimate organic carbon associated with metal cations and reactive mineral phases, *Soil Sci. Plant Nutr.*, 1–13, <https://doi.org/10.1080/00380768.2024.2448861>, 2025.
- Golchin, A., Oades, J. M., Skjemstad, J. O., and Clarke, P.: Study of free and occluded particulate organic matter in soils by solid state ^{13}C Cp/MAS NMR spectroscopy and scanning electron microscopy, *Aust. J. Soil Res.*, 32 (2), 285–309, <https://doi.org/10.1071/SR9940285>, 1994.
- 1110 Goslee, S. C., and Urban, D. L.: The ecodist package for dissimilarity-based analysis of ecological data, *J. Stat. Softw.*, 22 (7), 1–19, <https://doi.org/10.18637/jss.v022.i07>, 2007.
- Gray, J., and Murphy, B.: Parent material and world soil distribution, in: Symposium no. 21, Proceedings of 17th World Congress of Soil Science, 2215, 1–14, 2002.
- 1115 Hall, S. J., Ye, C., Weintraub, S. R., and Hockaday, W. C.: Molecular trade-offs in soil organic carbon composition at continental scale, *Nat. Geosci.*, 13, 687–692, <https://doi.org/10.1038/s41561-020-0634-x>, 2020.
- Hall, S. J., and Thompson, A.: What do relationships between extractable metals and soil organic carbon concentrations mean?, *Soil Sci. Soc. Am. J.*, 86, 195–208, <https://doi.org/10.1002/saj2.20343>, 2022.
- 1120 Hara, S., Kakizaki, K., Bamba, M., Itakura, M., Sugawara, M., Suzuki, A., Sasaki, Y., Takeda, M., Tago, K., Ohbayashi, T., Aono, T., Aoyagi, L. N., Shimada, H., Shingubara, R., Masuda, S., Shibata, A., Shirasu, K., Wagai, R., Akiyama, H., Sato, S., and Minamisawa, K.: Does rhizobial inoculation change the microbial community in field soils? A comparison with agricultural land-use changes, *Microbes Environ.*, 39 (3), ME24006, <https://doi.org/10.1264/jsme2.ME24006>, 2024.
- Harter, R. D., and Naidu, R.: Role of metal-organic complexation in metal sorption by soils, *Adv. Agron.*, 55, 219–263, [https://doi.org/10.1016/S0065-2113\(08\)60541-6](https://doi.org/10.1016/S0065-2113(08)60541-6), 1995.
- 1125 Hartmann, M., and Six, J.: Soil structure and microbiome functions in agroecosystems, *Nat. Rev. Earth Environ.*, 4, 4–18, <https://doi.org/10.1038/s43017-022-00366-w>, 2023.
- Hatton, P. J., Kleber, M., Zeller, B., Moni, C., Plante, A. F., Townsend, K., Gelhaye, L., Lajtha, K., and Derrien, D.: Transfer of litter-derived N to soil mineral-organic associations: Evidence from decadal ^{15}N tracer experiments, *Org. Geochem.*, 42 (12), 1489–1501, <https://doi.org/10.1016/j.orggeochem.2011.05.002>, 2012.
- 1130 Heckman, K., Lawrence, C. R., and Harden, J. W.: A sequential selective dissolution method to quantify storage and stability of organic carbon associated with Al and Fe hydroxide phases, *Geoderma*, 312, 24–35, <https://doi.org/10.1016/j.geoderma.2017.09.043>, 2018.
- 1135 Heckman, K., Hicks Pries, C. E., Lawrence, C. R., Rasmussen, C., Crow, S. E., Hoyt, A. M., von Fromm, S. F., Shi, Z., Stoner, S., McGrath, C., Beem-Miller, J., Berhe, A. A., Blankinship, J. C., Keiluweit, M., Marín-Spiotta, E., Monroe, J. G., Plante, A. F., Schimel, J., Sierra, C. A., Thompson, A., and Wagai, R.: Beyond bulk: Density fractions explain heterogeneity in global soil carbon abundance and persistence, *Glob. Chang Biol.*, 28 (3), 1178–1196, <https://doi.org/10.1111/gcb.16023>, 2022.
- Hemingway, J. D., Rothman, D. H., Grant, K. E., Rosengard, S. Z., Eglinton, T. I., Derry, L. A., and Galy, V. V.: Mineral protection regulates long-term global preservation of natural organic carbon, *Nature*, 570, 228–231, <https://doi.org/10.1038/s41586-019-1280-6>, 2019.
- 1140 Hiradate, S., Nakadai, T., Shindo, H., and Yoneyama, T.: Carbon source of humic substances in some Japanese volcanic ash soils determined by carbon stable isotopic ratio, $\delta^{13}\text{C}$, *Geoderma*, 119 (1–2), 133–141, [35](https://doi.org/10.1016/S0016-</p>
</div>
<div data-bbox=)

7061(03)00257-X, 2004.

Hitchcock, A. P.: aXis 2000 - Analysis of X-ray Images and Spectra, <http://unicorn.mcmaster.ca/aXis2000.html>, 2023.

1145

Horie, Y., Iwasaki, A., Tomoyose, N., Kido, M., Yamaguchi, T., Tada, K., Kawashita, H., Kohno, A., Hamamura, K., Yamazoe, R., Matsumoto, R., Yokoyama, S., Noguchi, I., Yagoh, H., Kai, I., Hamano, A., and Yoshida, F.: Acid deposition survey in Japan, phase 5 (2016). *Journal of Environmental Laboratories Association*, 41 (3), 2–37, <http://db.cger.nies.go.jp/dataset/acidrain/ja/05/>, 2016. (in Japanese).

1150

Hughes, J. C.: High gradient magnetic separation of some soil clays from Nigeria, Brazil and Colombia. I. The interrelationships of iron and aluminium extracted by acid ammonium oxalate and carbon. *Eur. J. Soil Sci.*, 33, 509–519, <https://doi.org/10.1111/j.1365-2389.1982.tb01785.x>, 1982.

IUSS Working Group WRB (Eds.): World Reference Base for Soil Resources 2014, update 2015: International soil classification system for naming soils and creating legends for soil maps, World Soil Resources Reports No. 106, FAO, Rome, 2015.

1155

Jamoteau, F., Cam, N., Levard, C., Doelsch, E., Gassier, G., Duvivier, A., Boulineau, A., Saint-Antonin, F., and Basile-Doelsch, I.: Structure and chemical composition of soil C-rich Al–Si–Fe coprecipitates at nanometer scale, *Environ. Sci. Technol.*, 57 (49), 20615–20626, <https://doi.org/10.1021/acs.est.3c06557>, 2023.

1160

Jamoteau, F., Doelsch, E., Cam, N., Levard, C., Woignier, T., Boulineau, A., Saint-Antonin, F., Swaraj, S., Gassier, G., Duvivier, A., Borschneck, D., Pons, M-L., Chaurand, P., Vidal, V., Brouilly, N., and Basile-Doelsch, I.: Interplay of coprecipitation and adsorption processes: deciphering amorphous mineral–organic associations under both forest and cropland conditions, *SOIL*, 11 (2), 535–552, <https://doi.org/10.5194/soil-11-535-2025>, 2025.

Kaiser, K., Guggenberger, G., Haumaier, L., and Zech, W.: Dissolved organic matter sorption on subsoils and minerals studied by ¹³C-NMR and DRIFT spectroscopy. *Eur. J. Soil Sci.* 48 (2), 301–310, <https://doi.org/10.1111/j.1365-2389.1997.tb00550.x>, 1997.

1165

Keil, R. G., and Mayer, L. M.: Mineral matrices and organic matter, in: *Treatise on Geochemistry (Second Edition)*, edited by: Holland, H. D., and Turekian, K. K., Elsevier, 337–359, <https://doi.org/10.1016/B978-0-08-095975-7.01024-X>, 2014.

Kleber, M., Eusterhues, K., Keiluweit, M., Mikutta, C., Mikutta, R., and Nico, P. S.: Chapter one - mineral–organic associations: Formation, properties, and relevance in soil environments, in: *Advances in Agronomy*, edited by: Sparks, D. L., Academic Press, Volume 130, 1–140, <https://doi.org/10.1016/bs.agron.2014.10.005>, 2015.

1170

Koba, K., Kinoshita, K., Onishi, Y., Fukushima, K., Osaka, K., Matsuo, N., Funakawa, K., Seko, Y., Medo, A., Hirasawa, R., O Ogawa, N., Hyodo, F., and Yoshimizu, C.: Carbon and nitrogen isotope analysis on small samples using a near-conventional EA-IRMS system, *Radioisotopes*, 70 (4), 291–299, <https://doi.org/10.3769/radioisotopes.70.291>, 2021. (in Japanese).

1175

Krause, L., Biesgen, D., Treder, A., Schweizer, S. A., Klumpp, E., Knief, C., and Siebers, N.: Initial microaggregate formation: Association of microorganisms to montmorillonite-goethite aggregates under wetting and drying cycles, *Geoderma*, 351, 250–260, <https://doi.org/10.1016/j.geoderma.2019.05.001>, 2019.

Lawrence, C. R., Harden, J. W., Xu, X., Schulz, M. S., and Trumbore, S. E.: Long-term controls on soil organic carbon with depth and time: A case study from the Cowlitz River Chronosequence, WA USA, *Geoderma*, 247–248, 73–87, <https://doi.org/10.1016/j.geoderma.2015.02.005>, 2015.

1180

Lehmann, J., Bossio, D. A., Kögel-Knabner, I., and Rillig, M. C.: The concept and future prospects of soil health, *Nat. Rev. Earth Environ.*, 1, 544–553, <https://doi.org/10.1038/s43017-020-0080-8>, 2020.

Liu, C., Cui, Y., Li, X., and Yao, M.: microeco: an R package for data mining in microbial community ecology, *FEMS Microbiol. Ecol.*, 97 (2), fiae255, <https://doi.org/10.1093/femsec/fiae255>, 2021.

Lundström, U. S., van Breemen, N., and Bain, D.: The podzolization process. A review, *Geoderma*, 94 (2–4), 91–107, [https://doi.org/10.1016/S0016-7061\(99\)00036-1](https://doi.org/10.1016/S0016-7061(99)00036-1), 2000.

- 1185 Lybrand, R. A., Austin, J. C., Fedenko, J., Gallery, R. E., Rooney, E., Schroeder, P. A., Zaharescu, D. G., and Qafoku, O.: A coupled microscopy approach to assess the nano-landscape of weathering, *Sci. Rep.*, 9, 5377, <https://doi.org/10.1038/s41598-019-41357-0>, 2019.
- Mao, X., Van Zwieten, L., Zhang, M., Qiu, Z., Yao, Y., and Wang, H.: Soil parent material controls organic matter stocks and retention patterns in subtropical China, *J. Soils Sediments*, 20, 2426–2438, <https://doi.org/10.1007/s11368-020-02578-3>, 2020.
- 1190 Martinelli, L. A., Piccolo, M. C., Townsend, A. R., Vitousek, P. M., Cuevas, E., McDowell, W., Robertson, G. P., Santos, O. C., and Treseder, K.: Nitrogen stable isotopic composition of leaves and soil: Tropical versus temperate forests, *Biogeochemistry*, 46, 45–65, <https://doi.org/10.1007/BF01007573>, 1999.
- Masiello, C. A., Chadwick, O. A., Southon, J., Torn, M. S., and Harden, J. W.: Weathering controls on mechanisms of carbon storage in grassland soils, *Global Biogeochem. Cycles*, 18, GB4023, <https://doi.org/10.1029/2004GB002219>, 2004.
- 1195 McMurdie, P. J., and Holmes, S.: phyloseq: An R package for reproducible interactive analysis and graphics of microbiome census data, *PLoS ONE*, 8 (4), e61217, <https://doi.org/10.1371/journal.pone.0061217>, 2013.
- Moni, C., Derrien, D., Hatton, P. J., Zeller, B., and Kleber, M.: Density fractions versus size separates: Does physical fractionation isolate functional soil compartments?, *Biogeosciences*, 9 (12), 5181–5197, <https://doi.org/10.5194/bg-9-5181-2012>, 2012.
- 1200 [Oades, J.M. The retention of organic matter in soils. Vol. 5 Issue 1 Pages 35-70, https://doi.org/ 10.1007/BF02180317, Biogeochemistry, 1988.](https://doi.org/10.1007/BF02180317)
- Ogawa, N. O., Nagata, T., Kitazato, H., and Ohkouchi, N.: Ultra-sensitive elemental analyzer/isotope ratio mass spectrometer for stable nitrogen and carbon isotope analyses, in: *Earth, Life and Isotopes*, edited by: Ohkouchi, N., Tayasu, I., and Koba, K., Kyoto University Press, Kyoto, Japan, 339–353. ISBN: 9784876989607, 2010.
- 1205 Oksanen, J.: *Vegan: ecological diversity*. R project, 368, 1–11, <https://cran.r-project.org/web/packages/vegan/vignettes/diversity-vegan.pdf>, 2013.
- Orgill, S. E., Condon, J. R., Conyers, M. K., Morris, S. G., Murphy, B. W., and Greene, R. S. B.: Parent material and climate affect soil organic carbon fractions under pastures in south-eastern Australia, *Soil Res.*, 55 (8), 799–808, <https://doi.org/10.1071/SR16305>, 2017.
- 1210 Parker, D. R.: Aluminum speciation, in: *Encyclopedia of Soils in the Environment*, edited by: Hillel, D., Elsevier, 50–56, <https://doi.org/10.1016/B0-12-348530-4/00199-5>, 2005.
- Percival, H. J., Parfitt, R. L., and Scott, N. A.: Factors controlling soil carbon levels in New Zealand grasslands is clay content important?, *Soil Sci. Soc. Am. J.*, 64 (5), 1623–1630, <https://doi.org/10.2136/sssaj2000.6451623x>, 2000.
- 1215 Philippot, L., Chenu, C., Kappler, A., Rillig, M. C., and Fierer, N.: The interplay between microbial communities and soil properties, *Nat. Rev. Microbiol.*, 22, 226–239, <https://doi.org/10.1038/s41579-023-00980-5>, 2024.
- Possinger, A. R., Zachman, M. J., Enders, A., Levin, B. D. A., Muller, D. A., Kourkoutis, L. F., and Lehmann, J.: Organo–organic and organo–mineral interfaces in soil at the nanometer scale, *Nat. Commun.*, 11, 6103, <https://doi.org/10.1038/s41467-020-19792-9>, 2020.
- 1220 Prietzel, J., Müller, S., Kögel-Knabner, I., Thieme, J., Jaye, C., and Fischer, D.: Comparison of soil organic carbon speciation using C NEXAFS and CPMAS ¹³C NMR spectroscopy, *Sci. Total Environ.*, 628–629, 906–918, <https://doi.org/10.1016/j.scitotenv.2018.02.121>, 2018.
- Pronk, G. J., Heister, K., Vogel, C., Babin, D., Bachmann, J., Ding, G. C., Ditterich, F., Gerzabek, M. H., Giebler, J., Hemkemeyer, M., Kandeler, E., Mouvenchery, Y. K., Miltner, A., Poll, C., Schaumann, G. E., Smalla, K., Steinbach, A., Tanuwidjaja, I., Tebbe, C. C., Wick, L. Y., Woche, S. K., Totsche, K. U., Schloter, M., and Kögel-Knabner, I.: Interaction of minerals, organic matter, and microorganisms during biogeochemical interface formation as shown by a series of
- 1225

artificial soil experiments, *Biol. Fertil. Soils*, 53, 9–22, <https://doi.org/10.1007/s00374-016-1161-1>, 2017.

Rabot, E., Wiesmeier, M., Schlüter, S., and Vogel, H. -J.: Soil structure as an indicator of soil functions: A review,

1230 *Geoderma*, 314, 122–137, <https://doi.org/10.1016/j.geoderma.2017.11.009>, 2018.

Rasmussen, C., Heckman, K., Wieder, W. R., Keiluweit, M., Lawrence, C. R., Berhe, A. A., Blankinship, J. C., Crow, S. E., Druhan, J. L., and Pries, C. E. H. et al.: Beyond clay: towards an improved set of variables for predicting soil organic matter content, *Biogeochemistry*, 137, 297–306, <https://doi.org/10.1007/s10533-018-0424-3>, 2018.

1235 Rasmussen, C., Torn, M. S., and Southard, R. J.: Mineral assemblage and aggregates control carbon dynamics in a California conifer forest, *Soil Sci. Soc. Am. J.*, 69 (6), 1711–1721, <https://doi.org/10.2136/sssaj2005.0040>, 2005.

Regelink, I. C., Stoof, C. R., Rousseva, S., Weng, L., Lair, G. J., Kram, P., Nikolaidis, N. P., Kercheva, M., Banwart, S., and Comans, R. N. J.: Linkages between aggregate formation, porosity and soil chemical properties, *Geoderma*, 247–248, 24–37, <https://doi.org/10.1016/j.geoderma.2015.01.022>, 2015.

1240 Rennert, T.: Wet-chemical extractions to characterise pedogenic Al and Fe species – a critical review, *Soil Res.*, 57, 1–16, <https://doi.org/10.1071/SR18299>, 2019.

[Rowley, M. C., Nico, P. S., Bone, S. E., Marcus, M. A., Pegoraro, E. F., Castanha, C., Kang, K., Bhattacharyya, A., and Torn, M. S.: Association between soil organic carbon and calcium in acidic grassland soils from Point Reyes National Seashore, CA Peña, Jasquelin, *Biogeochemistry*, 165, 91–111, <https://doi.org/10.1007/s10533-023-01059-2>, 2023.](#)

1245 Saidy, A. R., Smernik, R. J., Baldock, J. A., Kaiser, K., and Sanderman, J.: Microbial degradation of organic carbon sorbed to phyllosilicate clays with and without hydrous iron oxide coating, *Eur. J. Soil Sci.*, 66 (1), 83–94, <https://doi.org/10.1111/ejss.12180>, 2015.

[Schlüter, S., Sammartino, S., and Koestel, J.: Exploring the relationship between soil structure and soil functions via pore-scale imaging, *Geoderma*, 370, 114370, <https://doi.org/10.1016/j.geoderma.2020.114370>, 2020.](#)

1250 Schneider, M. P. W., Scheel, T., Mikutta, R., van Hees, P., Kaiser, K., and Kalbitz, K.: Sorptive stabilization of organic matter by amorphous Al hydroxide, *Geochim. Cosmochim. Acta.*, 74, 1606–1619, <https://doi.org/10.1016/j.gca.2009.12.017>, 2010.

Shang, C., and Tiessen, H.: Organic matter stabilization in two semiarid tropical soils: Size, density, and magnetic separations, *Soil Sci. Soc. Am. J.*, 62 (5), 1247–1257, <https://doi.org/10.2136/sssaj1998.03615995006200050015x>, 1998.

1255 Shimada, H., Wagai, R., Inoue, Y., Tamura, K., and Asano, M.: Millennium timescale carbon stability in an Andisol: How persistent are organo-metal complexes?, *Geoderma*, 417, 115820, <https://doi.org/10.1016/j.geoderma.2022.115820>, 2022.

Soil Survey Staff. (Eds.): Keys to Soil Taxonomy, 12th ed, USDA-Natural Resources Conservation Service, Washington, DC, 2014.

1260 Sokol, N. W., Sohng, J., Moreland, K., Slessarev, E., Goertzen, H., Schmidt, R., Samaddar, S., Holzer, I., Almaraz, M., Geoghegan, E., Houlton, B., Montañez, I., Pett-Ridge, J., and Scow, K.: Reduced accrual of mineral-associated organic matter after two years of enhanced rock weathering in cropland soils, though no net losses of soil organic carbon, *Biogeochemistry*, 167, 989–1005, <https://doi.org/10.1007/s10533-024-01160-0>, 2024.

Sollins, P., Homann, P., and Caldwell, B. A.: Stabilization and destabilization of soil organic matter: mechanisms and controls, *Geoderma*, 74 (1–2), 65–105, [https://doi.org/10.1016/S0016-7061\(96\)00036-5](https://doi.org/10.1016/S0016-7061(96)00036-5), 1996.

1265 Sollins, P., Kramer, M. G., Swanston, C., Lajtha, K., Filley, T., Aufdenkampe, A. K., Wagai, R., and Bowden, R. D.: Sequential density fractionation across soils of contrasting mineralogy: Evidence for both microbial- and mineral-controlled soil organic matter stabilization, *Biogeochemistry*, 96, 209–231, <https://doi.org/10.1007/s10533-009-9359-z>, 2009.

1270 Solomon, D., Lehmann, J., Harden, J., Wang, J., Kinyangi, J., Heymann, K., Karunakaran, C., Lu, Y., Wirrick, S., and Jacobsen, C.: Micro- and nano-environments of carbon sequestration: Multi-element STXM–NEXAFS spectromicroscopy assessment of microbial carbon and mineral associations, *Chem. Geol.*, 329, 53–73,

<https://doi.org/10.1016/j.chemgeo.2012.02.002>, 2012.

Sørensen, L. H.: Stabilization of newly formed amino acid metabolites in soil by clay minerals, *Soil Sci.*, 114 (1), 5–11, <https://doi.org/10.1097/00010694-197207000-00002>, 1972.

1275

Suzuki, M. T., Taylor, L. T., and DeLong, E. F.: Quantitative analysis of small-subunit rRNA genes in mixed microbial populations via 5'-nuclease assays. *Appl. Environ. Microbiol.*, 66 (11), 4605–4614, <https://doi.org/10.1128/AEM.66.11.4605-4614.2000>, 2000.

Takahashi, T., and Dahlgren, R. A.: Nature, properties and function of aluminum–humus complexes in volcanic soils, *Geoderma*, 263, 110–121, <https://doi.org/10.1016/j.geoderma.2015.08.032>, 2016.

1280

Takeichi, Y., Inami, N., Suga, H., Miyamoto, C., Ueno, T., Mase, K., Takahashi, Y., and Ono, K.: Design and performance of a compact scanning transmission X-ray microscope at the Photon Factory, *Rev. Sci. Instrum.*, 87 (1), 013704, <https://doi.org/10.1063/1.4940409>, 2016.

Tamrat, W. Z., Rose, J., Grauby, O., Doelsch, E., Levard, C., Chaurand, P., and Basile-Doelsch, I.: Composition and molecular scale structure of nanophases formed by precipitation of biotite weathering products, *Geochim. Cosmochim. Acta*, 229, 53–64, <https://doi.org/10.1016/j.gca.2018.03.012>, 2018.

1285

Tamrat, W. Z., Rose, J., Grauby, O., Doelsch, E., Levard, C., Chaurand, P., and Basile-Doelsch, I.: Soil organo-mineral associations formed by co-precipitation of Fe, Si and Al in presence of organic ligands, *Geochim. Cosmochim. Acta*, 260, 15–28, <https://doi.org/10.1016/j.gca.2019.05.043>, 2019.

Tipping, E.: The adsorption of aquatic humic substances by iron oxides, *Geochim. Cosmochim. Acta*, 45 (2), 191–199, [https://doi.org/10.1016/0016-7037\(81\)90162-9](https://doi.org/10.1016/0016-7037(81)90162-9), 1981.

1290

Torn, M. S., Trumbore, S. E., Chadwick, O. A., Vitousek, P. M., and Hendricks, D. M.: Mineral control of soil organic carbon storage and turnover, *Nature*, 389, 170–173, <https://doi.org/10.1038/38260>, 1997.

Totsche, K. U., Amelung, W., Gerzabek, M. H., Guggenberger, G., Klumpp, E., Knief, C., Lehdorff, E., Mikutta, R., Peth, S., Prechtel, A., Ray, N., and Kögel-Knabner, I.: Microaggregates in soils, *J. Plant Nutr. Soil Sci.*, 181, 104–136, <https://doi.org/10.1002/jpln.201600451>, 2018.

1295

Underwood, T. R., Bourg, I. C., and Rosso, K. M.: Mineral-associated organic matter is heterogeneous and structured by hydrophobic, charged, and polar interactions, *PNAS*, 121 (46), e2413216121, <https://doi.org/10.1073/pnas.2413216121>, 2024.

Uroz, S., Kelly, L. C., Turpault, M. P., Lepleux, C., and Frey-Klett, P.: The mineralosphere concept: Mineralogical control of the distribution and function of mineral-associated bacterial communities, *Trends Microbiol.*, 23 (12), 751–762, <https://doi.org/10.1016/j.tim.2015.10.004>, 2015.

1300

Vogel, C., Babin, D., Pronk, G. J., Heister, K., Smalla, K., and Kögel-Knabner, I.: Establishment of macro-aggregates and organic matter turnover by microbial communities in long-term incubated artificial soils, *Soil Biol. Biochem.*, 79, 57–67, <https://doi.org/10.1016/j.soilbio.2014.07.012>, 2014.

von Fromm, S. F., Hoyt, A. M., Lange, M., Acquah, G. E., Aynekulu, E., Berhe, A. A., Haefele, S. M., McGrath, S. P., Shepherd, K. D., Sila, A. M., Six, J., Towett, E. K., Trumbore, S. E., Vågen, T.-G., Weullow, E., Winowiecki, L. A., and Doetterl, S.: Continental-scale controls on soil organic carbon across sub-Saharan Africa, *SOIL*, 7, 305–332, <https://doi.org/10.5194/soil-7-305-2021>, 2021.

1305

von Fromm, S. F., Jungkunst, H. F., Amenkhienan, B., Hall, S. J., Georgiou, K., Pries, C. H., Montaña-López, F., Quesada, C. A., Rasmussen, C., Schrupf, M., Singh, B., Thompson, A., Wagai, R., and Fiedler, S.: Moisture and soil depth govern relationships between soil organic carbon and oxalate-extractable metals at the global scale, *Biogeochemistry*, 168, 20, <https://doi.org/10.1007/s10533-025-01208-9>, 2025.

1310

Wagai, R., and Sollins, P.: Biodegradation and regeneration of water-soluble carbon in a forest soil: Leaching column study, *Biol. Fertil. Soils*, 35, 18–26, <https://doi.org/10.1007/s00374-001-0434-4>, 2002.

- 1315 Wagai, R., and Mayer, L.M.: Sorptive stabilization of organic matter in soils by hydrous iron oxides, *Geochim. Cosmochim. Acta*, 71 (1), 25–35, <https://doi.org/10.1016/j.gca.2006.08.047>, 2007.
- Wagai, R., Kishimoto-Mo, A. W., Yonemura, S., Shirato, Y., Hiradate, S., and Yagasaki, Y.: Linking temperature sensitivity of soil organic matter decomposition to its molecular structure, accessibility, and microbial physiology, *Glob. Chang. Biol.*, 19 (4), 1114–1125, <https://doi.org/10.1111/gcb.12112>, 2013a.
- 1320 Wagai, R., Mayer, L. M., Kitayama, K., and Shirato, Y.: Association of organic matter with iron and aluminum across a range of soils determined via selective dissolution techniques coupled with dissolved nitrogen analysis, *Biogeochemistry*, 112, 95–109, <https://doi.org/10.1007/s10533-011-9652-5>, 2013b.
- Wagai, R., Kajiura, M., Asano, M., and Hiradate, S.: Nature of soil organo-mineral assemblage examined by sequential density fractionation with and without sonication: Is allophanic soil different?, *Geoderma*, 241–242, 295–305, <https://doi.org/10.1016/j.geoderma.2014.11.028>, 2015.
- 1325 Wagai, R., Kajiura, M., Uchida, M., and Asano, M.: Distinctive roles of two aggregate binding agents in allophanic Andisols: Young carbon and poorly-crystalline metal phases with old carbon, *Soil Syst.*, 2 (2), 29, <https://doi.org/10.3390/soilsystems2020029>, 2018.
- Wagai, R., Kajiura, M., and Asano, M.: Iron and aluminum association with microbially processed organic matter via meso-density aggregate formation across soils: Organo-metallic glue hypothesis, *SOIL*, 6 (2), 597–627, <https://doi.org/10.5194/soil-6-597-2020>, 2020.
- 1330 Wagai, R., Yang, P. T., and Kaiser, K.: Interfacial reactions of microorganisms with minerals and organic matter, in: *Encyclopedia of Soils in the Environment (Second Edition)*, edited by: Goss, M. J., and Oliver, M., Academic Press, 458–469, <https://doi.org/10.1016/B978-0-12-822974-3.00232-9>, 2023.
- Wan, J., Tylliszczak, T., and Tokunaga, T. K.: Organic carbon distribution, speciation, and elemental correlations within soil microaggregates: Applications of STXM and NEXAFS spectroscopy, *Geochim. Cosmochim. Acta*, 71 (22), 5439–5449, <https://doi.org/10.1016/j.gca.2007.07.030>, 2007.
- 1335 Watanabe, T., Harsh, J. B., and Wagai, R.: Short-range ordered aluminosilicates, in: *Encyclopedia of Soils in the Environment (Second Edition)*, edited by: Goss, M. J., and Oliver, M., Academic Press, 121–134, <https://doi.org/10.1016/B978-0-12-822974-3.00223-8>, 2023.
- 1340 Wattel-Koekkoek, E. J. W., Buurman, P., Van der Plicht, J., Wattel, E., and Van Breemen, N.: Mean residence time of soil organic matter associated with kaolinite and smectite, *Eur. J. Soil Sci.*, 54 (2), 269–278, <https://doi.org/10.1046/j.1365-2389.2003.00512.x>, 2003.
- Xu, T., Yuan, Z., Vicca, S., Goll, D. S., Li, G., Lin, L., Chen, H., Bi, B., Chen, Q., Li, C., Wang, X., Wang, C., Hao, Z., Fang, Y., and Beerling, D. J.: Enhanced silicate weathering accelerates forest carbon sequestration by stimulating the soil mineral carbon pump, *Glob. Change Biol.*, 30 (8), e17464, <https://doi.org/10.1111/gcb.17464>, 2024.
- 1345 Yan, Y., Dong, X., Li, R., Zhang, Y., Yan, S., Guan, X., Yang, Q., Chen, L., Fang, Y., Zhang, W., and Wang, S.: Wollastonite addition stimulates soil organic carbon mineralization: Evidences from 12 land-use types in subtropical China, *Catena*, 225, 107031, <https://doi.org/10.1016/j.catena.2023.107031>, 2023.
- 1350 ~~Yang et al., under review~~ [Yang, P. T., Kurokawa, K., Nakao, A., Matsumura, E., and Wagai, R.: The potential of enhanced rock weathering for CO₂ removal and soil organic carbon storage via organo-mineral aggregation: the trade-off induced by basaltic rock particle size. *Biogeochemistry*, 169, 9, <https://doi.org/10.1007/s10533-025-01296-7>, 2026.](https://doi.org/10.1007/s10533-025-01296-7)
- Yudina, A., and Kuzyakov, Y.: Dual nature of soil structure: The unity of aggregates and pores, *Geoderma*, 434, 116478, <https://doi.org/10.1016/j.geoderma.2023.116478>, 2023.